Mon. Not. R. Astron. Soc. **000**, 1–32 (0000) Printed 11 November 2018 (MN LATEX style file v2.2)

Explicit relations and criteria for eclipses, transits and occultations

Dimitri Veras[1,2⋆†]
[1] *Centre for Exoplanets and Habitability, University of Warwick, Coventry CV4 7AL, UK*
[2] *Department of Physics, University of Warwick, Coventry CV4 7AL, UK*

11 November 2018

ABSTRACT

Solar system, exoplanet and stellar science rely on transits, eclipses and occultations for dynamical and physical insight. Often, the geometry of these configurations are modelled by assuming a particular viewpoint. Here, instead, I derive user-friendly formulae from first principles independent of viewpoint and in three dimensions. I generalise the results of Veras & Breedt (2017) by (i) characterising three-body systems which are in transit but are not necessarily perfectly aligned, and by (ii) incorporating motion. For a given snapshot in time, I derive explicit criteria to determine whether a system is in or out of transit, if an eclipse is total or annular, and expressions for the size of the shadow, including their extreme values and a condition for engulfment. These results are exact. For orbital motion, I instead obtain approximate results. By assuming fixed orbits, I derive a single implicit algebraic relation which can be solved to obtain the frequency and duration of transit events – including ingresses and egresses – for combinations of moons, planets and stars on arbitrarily inclined circular orbits; the eccentric case requires the solution of Kepler's equation but remains algebraic. I prove that a transit shadow – whether umbral, antumbral or penumbral – takes the shape of a parabolic cylinder, and finally present geometric constraints on Earth-based observers hoping to detect a three-body syzygy (or perfect alignment) – either in extrasolar systems or within the solar system – potentially as a double annular eclipse.

Key words: eclipses – transits – occultations – celestial mechanics – methods: analytical – planets and satellites: general

1 INTRODUCTION

Rovers on Mars, humans on Earth, and artificial satellites in space all have the capacity to view transits, eclipses and occultations of moons, planets and/or stars. In a similar vein, extrasolar observers may detect the Earth and other solar system planets through photometric events (Brakensiek & Ragozzine 2016; Heller & Pudritz 2016; Wells et al. 2018). These varied situations all feature the same basic geometry, independent of viewpoint: the intersection of a radiation cone with spheres (Cayley 1870; Rigge 1924). Consequently, a thorough exploration of this geometry might reveal widely-applicable results.

Previous investigations of this architecture have targeted specific groups of observers. For Earth-bound viewers of solar system-based transit phenomena, the annual Astronomical Almanac (USNO & HMNAO 2018) provides detailed numerical data. Ismail et al. (2015) supplied an analytical alternative incorporating Solar radiation pressure and Earth's oblateness, and Kawauchi et al. (2018) highlighted the importance of analysing Earth's transmission spectra during a lunar eclipse with both umbral and penumbral data. Ground-based observatories on Earth have also utilised stellar occultations to constrain minor planet shape (Ortiz et al. 2017) and ring particle size (e.g. Colwell et al. 2018; Mentel et al. 2018), but have difficulty distinguishing amongst grazing, partial and total eclipses in binary star systems (Morris 1999). For the external observers of solar system planets, Wells et al. (2018) instead derived non-grazing transit visibility zones, whereas Heller & Pudritz (2016) focused on the Earth's transit visibility zone.

In the field of extrasolar planets, Cabrera & Schneider (2007) considered the cone-sphere intersection in the context of flux changes and probabilities from imaging and reflected light. Exoplanet-based photometric transits include an extensive literature, with analytic treatments provided by Schneider & Chevreton

⋆ E-mail: d.veras@warwick.ac.uk
† STFC Ernest Rutherford Fellow

(1990), Seager & Mallén-Ornelas (2003), Tingley & Sackett (2005), Kipping (2008), Kipping (2010), Stevens & Gaudi (2013), Winn (2014), Martin & Triaud (2015), Luger et al. (2017), Martin (2017a) and Read et al. (2017). Related are transit timing variations (e.g. Ford et al. 2011; Agol & Fabrycky 2017), for which analytic work (Agol et al. 2005; Nesvorný & Morbidelli 2008; Nesvorný 2009; Lithwick et al. 2012; Deck & Agol 2015; Agol & Deck 2016; Hadden & Lithwick 2016) has also yielded fruitful results. Although exoplanetary literature rarely distinguishes umbral, penumbral, and antumbral cases from one another, recently Berzosa Molina et al. (2018) have analysed these different cases in flux and polarization phase curves of exoplanets with orbiting exomoons.

Here I take a step back and make no assumptions about the observer. I generalise the results of Veras & Breedt (2017) (hereafter Paper I), who characterised the geometry of syzygy – a situation when at least three bodies are co-linear. Now I consider non-syzygetic transits, and henceforth for simplicity largely use the word "transits" to refer also to eclipses and occultations[1].

In particular, my exploration seeks to establish what formulae can be derived from knowledge of only the radii and spatial locations of the three bodies involved in the transit. My assumptions are limited to (i) bodies being perfect spheres, and (ii) that light does not bend. I consider the darkest central shadows – the umbral and antumbral shadows – first, before moving onto the lighter peripheral penumbral shadows. Further, I consider motion. By assuming fixed orbits, I show how to compute frequencies and durations without having to solve differential equations.

1.1 Motivation for paper

The motivation for this paper arises from the benefits of a fully analytic treatment of eclipses, transits and occultations. The first benefit is speed and convenience: although running multi-body numerical simulations can occasionally be faster than evaluations of analytic treatments which involve long series expansions or differential equations, no series expansions nor differential equations are given in this paper. Further, ready-to-use algebraic equations do not require the setup time and output processing involved when running multi-body simulations, particularly when objects are modelled as solid bodies and ray tracing would be required to compute, for example, the condition to be in or out of transit. The second benefit is a mathematical understanding of the results. For example, the maximum shadow size on a solid body does not occur at a necessarily obvious location. Also, a simple mathematical swap (shown later in the paper) allows one to derive results for partial eclipses just as easily as for total or annular eclipses. Without this knowledge, unnecessary effort might be expended in generating or modifying a numerical module to process partial eclipses.

[1] The Glossary of the Astronomical Almanac (USNO & HMNAO 2018) defines an *eclipse* as a "the occultation of a celestial body caused by its passage through the shadow cast by another body", a *transit*, in part, as "the passage of one celestial body in front of another of greater apparent diameter", an *occultation* as, in part, "the obscuration of one celestial body by another of greater apparent diameter", and a *syzygy*, as, in part, "a configuration where three or more celestial bodies are positioned approximately in a straight line in space".

1.2 Plan for paper

Section 2 describes my basic setup. Sections 3-7 then explore what can be deduced from a snapshot in time, whereas Section 8 covers time evolution. Extensions are then presented in Sections 9-10 before the summary in Section 11.

In particular, for snapshots in time, in Section 3, I derive the equation of the intersection of a cone and a sphere. This equation, in combination with the properties of quadrics (or quadratic curves), is then used to deduce the shape of the shadow (Section 4) and the condition to be in or out of transit (Section 5). Section 6 establishes a criteria to determine whether the eclipse is annular or total, a direct extension of a similar result from Paper I. Section 7 then extends the geometry of Paper I in order to determine the size of this shadow in all cases.

I introduce time evolution in Section 8 and in both Appendices A and B, and consider transit durations and frequencies in three specific cases: (i) arbitrarily eccentric, coplanar orbits (Section 8.1), (ii) circular, arbitrarily inclined orbits (Section 8.2) and (iii) circular coplanar orbits (Section 8.3). For each case I provide three subcases: when the transit includes (i) one star and two planets, (ii) two stars and one planet, and (iii) one moon, one planet and one star.

Section 9 discusses how all of these results can be applied to penumbral shadows with relative ease. Section 10 then extends my off-syzygy results to four bodies in special cases where I do fix an observer.

Figures 1 and 2 provide a preview of the goals of the paper up through Section 8, and summarises how to reach them. These figures may be used as a convenient reference and algorithm (allowing the reader to skip the details) for computing eclipse-, transit- and occultation-related quantities in planetary and stellar systems. The figures also illustrate four different physical situations involving stars, planets and moons for which my results are applicable.

All notation and geometry is consistent with that of Paper I, and I have taken considerable care to avoid variable conflicts. Every variable in both papers is identified for easy access in Tables 1-4.

2 PHYSICAL AND GEOMETRICAL SETUP

Throughout the paper I model three-body systems. Only in Section 10 do I add a fourth body, and in a limited capacity.

2.1 The three bodies: radii and distances

I consider all three bodies to be spheres, at least one of which is a star, denoted the "primary" and with a radius R_1. The other two bodies (the "occulter", and the "target") are denoted respectively R_2 and R_3, with $R_1 > R_2$ and $R_1 > R_3$. However, there are no constraints on the relative sizes of the occulter and target.

The centre of the primary is taken to reside at the origin

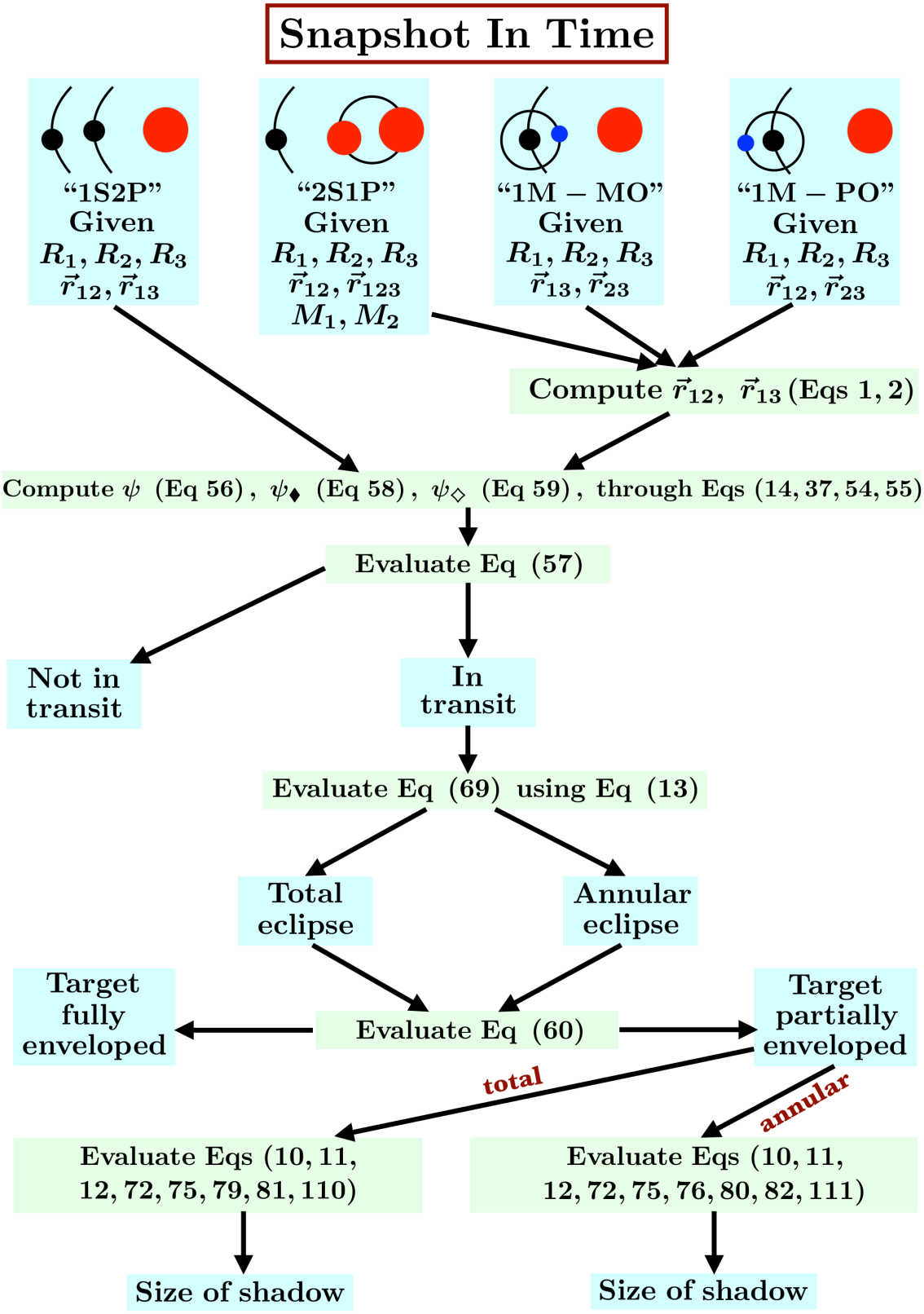

Figure 1. Procedure for obtaining results at snapshots in time. The four configurations shown are for two planets orbiting one star (1S2P), one planet orbiting two stars (1P2S), and one moon, one planet and one star with either the moon as the occulter (1M-MO) or the planet as the occulter (1M-PO). This flowchart demonstrates how one can determine with explicit expressions if three spherical bodies are in or out of transit, whether the eclipse is total or annular, whether the target is fully or partially engulfed in the shadow, and the size of the shadow.

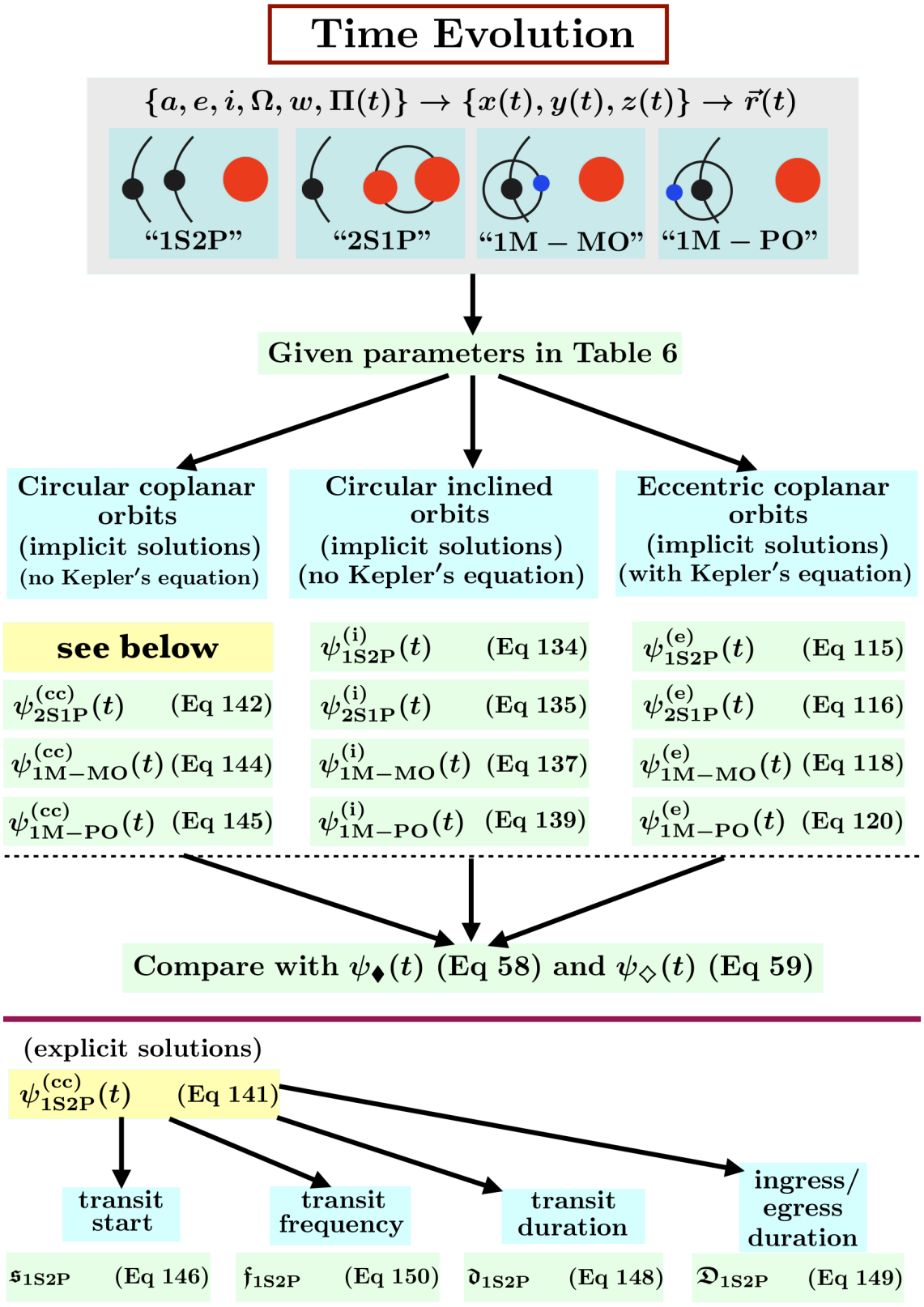

Figure 2. Procedure for obtaining results for motion along static orbits. The four configurations shown are the same as in Fig. 1. This flowchart illustrates how to obtain the frequency, duration and start times of transits and ingresses/egresses given sets of orbital elements.

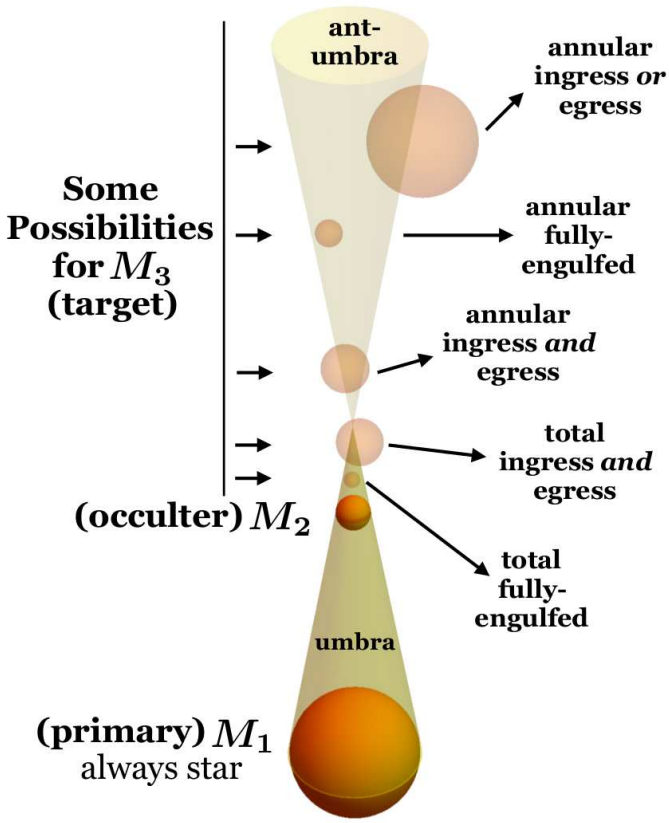

Figure 3. Potential configurations of three bodies in transit. The primary, which is always a star and the largest body, always forms a radiation cone with the occulter. If the target intersects this cone, then the target is said to be "in transit". If the near side of the target intersects the bottom nappe, the eclipse is total; otherwise, it is annular; the near side of the Earth, for example, lies coincidentally just at the vertex of the cone, which is why there are both annular and total solar eclipses. The entire target may or may not be completely engulfed in shadow. When not engulfed, as is the case for solar eclipses as seen on Earth, the target may be in ingress, egress or both, and the observability of the eclipse then depends on one's location on the target surface. The extension to the penumbral case – where a radiation cone is formed by internal tangent rays instead of external tangent rays – is covered in Section 9.

of an arbitrarily oriented orthogonal Cartesian $\{xyz\}$ coordinate system. The radiation from the primary always forms an umbral and antumbral cone with the occulter, as in Fig. 3. Note that this cone has two nappes (a nappe is one of the two sections of a double cone) and can move and change size during a transit. The target may be anywhere in space.

Only when the target intersects either or both nappes of the cone is a shadow formed. I refer to the side of the target facing the primary, where a shadow will be, as the "near side". The near side of the target could represent slightly more or slightly less than half of its total surface area (see e.g. equation A20 of Paper I). Whether the shadow results in a total or annular eclipse depends on which nappe contains the intersection of the target's near side (see Section 6).

At a given moment in time, I consider the target to be either fully engulfed inside of the cone, completely outside of the cone, or intersecting the cone. In this last case, if the surface of intersection occurs when the target is entering/leaving the cone, I denote those cases as ingress/egress. The target may be in both ingress and egress. Figure 3 illustrates many of the above possibilities.

Common examples can be visualised with the figure. For example, a total solar eclipse occurs when the Sun is the primary, the Moon is the occulter, the Earth is the target, and the Earth intersects the umbral cone. In this case, the Earth is usually is in both ingress and egress because of its relatively large size compared to the moon. Alternatively, an annular solar eclipse occurs when the Earth instead intersects the antumbral cone. For a lunar eclipse, the Earth becomes the occulter and the moon becomes the target.

Further, multiple planetary or stellar systems may be included: for example, an observer on Earth (the target) could see a distant star (the primary) being occulted by a Kuiper belt object (the occulter). For observing extrasolar planetary systems, one possibility is that the Earth is the target, the exoplanet is the occulter, and the exoplanet host star is the primary. Another possibility – when visualising what an extrasolar observer would see within, for example, a circumbinary system – is when the planet is the target, the smaller star is the occulter, and the larger star is the primary. For more examples, see Paper I.

The distance vector $\vec{r}$ always begins at the origin. Specific time-dependent distances are the distance between the centres of the primary and occulter $\vec{r}_{12}(t) = \{x_{12}(t), y_{12}(t), z_{12}(t)\}$, the primary and target $\vec{r}_{13}(t) = \{x_{13}(t), y_{13}(t), z_{13}(t)\}$ and the occulter and target

$$\vec{r}_{23}(t) = \vec{r}_{13}(t) - \vec{r}_{12}(t). \quad (1)$$

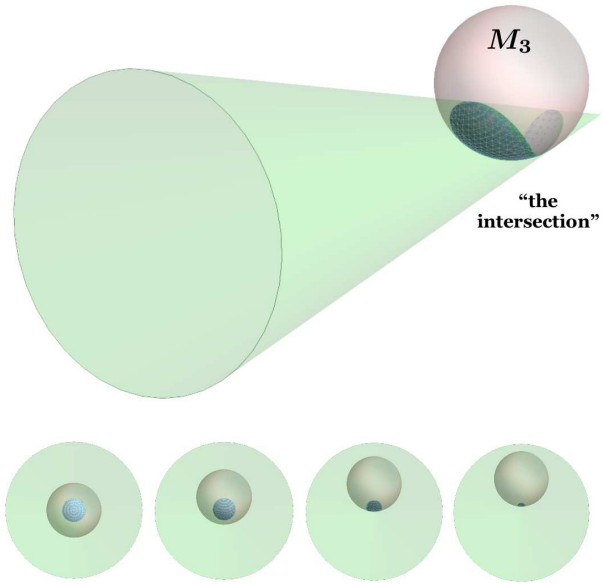

Figure 4. Visual representations of the intersection between the target and the radiation cone. The intersection is the meshed surface, and the shadow is the dark portion of that surface, which I prove is a parabolic cylinder in Section 4. The bottom four cartoons are from the same point of view, along the radiation cone axis, as the target gradually moves away from syzygy (left to right). These frames all demonstrate the case when the shadow does not engulf the target, much like in a solar eclipse; an observer would see the eclipse only by standing in the shadow. The true variation in the shadow size, however, can be obscured by adopting the fixed perspective here (see Section 7).

Henceforth, I will drop the denotation of the time dependence of these variables. As indicated in Fig. 1, for systems with two planets or stars, primarily $\vec{r}_{12}$ and $\vec{r}_{13}$ are used, whereas for systems with one moon, instead $\vec{r}_{13}$ and $\vec{r}_{23}$ are usually used.

Although the primary moves in time due to barycentric interactions, the origin of my coordinate system is always fixed on the primary's centre. Because of this barycentric motion, researchers often will define initial conditions in barycentric or Jacobi coordinates, particularly in circumbinary planetary systems. I denote the distance vector between the target and the barycentre of the primary and occulter as $\vec{r}_{123}$ with

$$\vec{r}_{13} = \vec{r}_{123} + \left(\frac{M_1}{M_1 + M_2}\right)\vec{r}_{12}. \tag{2}$$

In this expression, the masses of the primary and occulter are denoted as M_1 and M_2.

Finally, depending on the particular setup, one may reasonably adopt certain approximations. One example is when the target is somewhere in the Solar System and the primary is another stellar system. From Earth, one may observe either an exoplanetary transit or an occultation of a distant star across Saturn's rings. In the former case, one might assume $r_{12} \gg r_{13}, r_{23}$, whereas in the latter case, one might assume $r_{12}, r_{13} \gg r_{23}$. Regardless, I emphasise that in order to keep the analytical treatment as general as possible, no such approximations are made throughout the paper.

2.2 Orbital elements

In Paper I, only the radii and mutual distances of the three bodies were needed to be given in order to obtain their results (see their figure 5). The same is also true here for snapshots in time.

However, when I introduce motion, the number of initial parameters increases greatly: In that case, I also assume, in addition to all of the radii, a given set of the following orbital elements: $\{a, e, i, \Omega, w, \Pi\}$ for any two of the orbits. These elements are, respectively, semimajor axis (a), eccentricity (e), inclination (i), longitude of ascending node (Ω), argument of pericentre (w), and true anomaly (Π). This set uniquely defines r through:

$$r = \frac{a\left(1 - e^2\right)}{1 + e\cos\Pi} \tag{3}$$

which is independent of i, Ω, and w, and assumes that the orbit is an ellipse. However, the Cartesian components of r (which are x, y, and z) are individually dependent on i, Ω and w. Without loss of generality, I assume that the x-axis lies along the major axis of the ellipse, with the orbital pericentre being in the positive direction. Then

$$x = r\left[\cos\Omega\cos\left(w + \Pi\right) - \sin\Omega\sin\left(w + \Pi\right)\cos i\right], \tag{4}$$

$$y = r\left[\sin\Omega\cos\left(w + \Pi\right) + \cos\Omega\sin\left(w + \Pi\right)\cos i\right], \tag{5}$$

$$z = r\left[\sin\left(w + \Pi\right)\sin i\right]. \tag{6}$$

Because the systems in this paper all contain more than two bodies, mutual gravitational perturbations ensure that all of the orbital elements are time-dependent. Hence, the assumption of fixed orbits in this paper becomes weaker over longer timescales. I quantify the breakdown of this assumption for a few representative cases in Appendix B.

I will revisit motion along static orbits in Section 8. However, for now, I treat the snapshot case.

3 EXPRESSION FOR THE SHADOW

A transiting system will produce an antumbral or umbral shadow on the target. This shadow is defined as the intersection of the near side of the target with the cone. Figure 4 provides a cartoon which illustrates the near side of the target in shadow (the dark meshed region) and the far side of the target in the intersection but not the shadow (the light meshed region).

In order to obtain the equation describing the shadow, I first need to characterise the cone and sphere. The general Cartesian equations of both a sphere and a cone have quadratic terms. Because both shapes are translated from the origin, and the cone is arbitrarily oriented, these movements will introduce cross terms in the equations. Therefore, I express all equations as quadrics, also known as quadratic curves. These quadrics, whose properties are described in Smith (1884), Coolidge (1968), Zwillinger (1996) and McCrea (2006), have the form:

$$Ax^2 + By^2 + Cz^2 + 2Dxy + 2Eyz + 2Fxz + 2Gx + 2Hy + 2Jz + K = 0. \tag{7}$$

My immediate goal is to find expressions of the coefficients $(A, B, C, D, E, F, G, H, J, K)$ in terms

Table 1. Unstylised lowercase Roman variables used in this paper and in Paper I.

Variable	Explanation	Reference
a	Semimajor axis	
c	Auxiliary variable	Eq. A27 of Paper I
d	Height of penumbral cone	Eq. B4 of Paper I
e	Orbital eccentricity	
g	Fractional area of primary blocked out by occulter as seen by observer on target at syzygy	Eq. A30 of Paper I
h	Height of umbral cone	equation (11)
i	Orbital inclination	
j	Auxiliary variable	Eq. A28 of Paper I
k	Perpendicular distance with which fourth body is offset from a syzygy	Section 10 only
$k_\forall$	Critical value of k for which observer on fourth body cannot see a transit	equation (157)
$k_\sqcup$	Critical value of k for which target is entirely in the field of view of observer on fourth body	equation (160)
$k_\parallel$	Critical value of k for which occulter is entirely in the field of view of observer on fourth body	equation (163)
$k_\bullet$	Critical value of k to produce a double annular eclipse for observer on fourth body	equations (165-168)
l	Auxiliary variable	equations (165-169)
n	Distance between base of umbral cone and centre of primary	equation (13)
p	Transit number	equations (146-147)
$\vec{r}_{12}$	Distance vector between centres of primary and occulter	equations (1-2)
$\vec{r}_{13}$	Distance vector between centres of primary and target	equations (1-2)
$\vec{r}_{23}$	Distance vector between centres of occulter and target	equation (1)
$\vec{r}_{123}$	Distance vector between centre of target and barycentre of primary and occulter	equation (2)
$\vec{r}_{14}$	Distance vector between centres of primary and external body when the primary, occulter and target are in syzygy	Section 10 only
$r_{23}^\dagger$	Critical value of r_{23} within which target is engulfed in a total eclipse at syzygy	Eq. A10 of Paper I
$r_{23}^\ddagger$	Critical value of r_{23} beyond which target is engulfed in an annular eclipse at syzygy	Eq. A11 of Paper I
$r_{23}^\ominus$	Value of r_{23} such that the umbral shadow radius is equal to R_3 at syzygy	Eq. A21 of Paper I
r_{23}^*	Critical value of r_{23} beyond which target is engulfed in penumbral shadow at syzygy	Eq. B8 of Paper I
$r_{23}^\uplus$	Critical value of r_{23} beyond which target blocks primary's starlight for observer on fourth body who is colinear with a syzygy	equation (154)
$r_{23}^\bullet$	Critical value of r_{23} to produce a double annular eclipse for observer on fourth body who is offset with a syzygy	equation (170)
$r_{\rm loc}$	Distance between centre of primary and point on target surface	equation (68)
t	Time	
u	Distance between base of penumbral cone and centre of primary	Eq. B6 of Paper I
w	Argument of pericentre	
x	Cartesian component of $\vec{r}$	equation (4)
$x_{\rm loc}$	Cartesian component of point location on target surface	equation (63)
y	Cartesian component of $\vec{r}$	equation (5)
$y_{\rm loc}$	Cartesian component of point location on target surface	equation (64)
z	Cartesian component of $\vec{r}$	equation (6)
$z_{\rm loc}$	Cartesian component of point location on target surface	equation (65)

of $\{R_1, R_2, R_3, x_{12}, y_{12}, z_{12}, x_{13}, y_{13}, z_{13}\}$ (recall that the last six of these variables can be combined to yield $x_{23}, y_{23}, z_{23}, x_{123}, y_{123}$, and z_{123}).

3.1 Cartesian equation of the target

The general equation of the surface of the spherical target is

$$(x - x_{13})^2 + (y - y_{13})^2 + (z - z_{13})^2 = R_3^2. \tag{8}$$

When expressed as a quadric, this surface gives $A_{\rm tar} = B_{\rm tar} = C_{\rm tar} = 1$, $D_{\rm tar} = E_{\rm tar} = F_{\rm tar} = 0$, $G_{\rm tar} = -x_{13}$, $H_{\rm tar} = -y_{13}$, $J_{\rm tar} = -z_{13}$ and $K_{\rm tar} = r_{13}^2 - R_3^2$. This equation does not distinguish the near side from the far side of the target. I never have to consider the interior of this sphere.

3.2 Cartesian equation of the cone

A right circular cone with two nappes is always formed by the spherical primary and the spherical occulter, such that the vertex is outside of both bodies. The centre of the primary, which does not include the base of the cone, lies at

Table 2. Unstylised uppercase Roman variables used in this paper and in Paper I.

Variable	Explanation	Reference
A	Quadric coefficient of x^2	equation (7)
B	Quadric coefficient of y^2	equation (7)
C	Quadric coefficient of z^2	equation (7)
D	Half of quadric coefficient of xy	equation (7)
E	Half of quadric coefficient of yz	equation (7)
F	Half of quadric coefficient of xz	equation (7)
G	Half of quadric coefficient of x	equation (7)
H	Half of quadric coefficient of y	equation (7)
J	Half of quadric coefficient of z	equation (7)
K	Quadric constant term	equation (7)
M	Mass	
R_1	Radius of primary (always a star)	
R_2	Radius of occulter	
R_3	Radius of target	
R_4	Radius of fourth external body (only when other three are in syzygy)	Section 10 only
$R_{\rm c}$	Radius of base of umbral cone	equation (12)
$R_{\rm d}$	Radius of base of penumbral cone	Eq. B5 of Paper I
$R_{\rm ant}$	Antumbral shadow radius at syzygy	Eq. A23 of Paper I
$R_{\rm ant}^{\rm cen}$	Auxiliary variable	equation (90)
$R_{\rm ant}^{\rm edge}$	Auxiliary variable	equation (89)
$R_{\rm pen}$	Penumbral shadow radius at syzygy	Eq. B13 of Paper I
$R_{\rm umb}$	Umbral shadow radius at syzygy	Eq. A19 of Paper I
$R_{\rm umb}^{\rm cen}$	Auxiliary variable	equation (88)
$R_{\rm umb}^{\rm edge}$	Auxiliary variable	equation (87)
$S_{\rm ant}$	Antumbral surface area at syzygy	Eq. A25 of Paper I
$S_{\rm pen}$	Penumbral surface area at syzygy	Eq. B14 of Paper I
$S_{\rm umb}$	Umbral surface area at syzygy	Eq. A24 of Paper I

the origin of the coordinate system (see Fig. 5, which is a duplicate of Fig. A1 of Paper I).

In order to construct the equation of this cone in Cartesian (x, y, z) coordinates, consider first a different coordinate system $(\mathfrak{u}, \mathfrak{v}, \mathfrak{w})$. In this new coordinate system, imagine a right circular cone with (i) the vertex at the origin, (ii) a base which is arbitrarily oriented, and (iii) a semi-vertical angle α.

The equation of this cone is

$$\left(\mathfrak{u}^2 + \mathfrak{v}^2 + \mathfrak{w}^2\right)\cos^2\alpha = \left(\frac{x_{12}}{r_{12}}\mathfrak{u} + \frac{y_{12}}{r_{12}}\mathfrak{v} + \frac{z_{12}}{r_{12}}\mathfrak{w}\right)^2 \tag{9}$$

where I have inserted the direction cosines from my setup as the coefficients of $\mathfrak{u}$, $\mathfrak{v}$ and $\mathfrak{w}$. The semi-vertical angle α, as shown in Fig. 5, is given by

$$\tan\alpha = \frac{R_{\rm c}}{h} \tag{10}$$

where

$$h = R_1\left[\frac{r_{12}^2 - (R_1 - R_2)^2}{r_{12}\,(R_1 - R_2)}\right], \tag{11}$$

$$R_{\rm c} = \frac{R_1}{r_{12}}\sqrt{r_{12}^2 - (R_1 - R_2)^2}. \tag{12}$$

Equation (9) therefore reduces to a better result commonly found in textbooks in the special case of the cone's

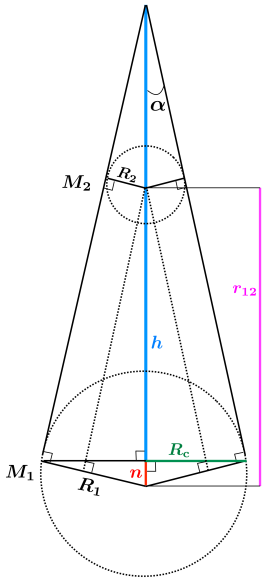

Figure 5. The radiation cone producing umbral and antumbral shadows; a reproduction of figure A1 from Paper I but with the inclusion of the semi-vertical angle α. This figure helps illustrate the geometric meaning of h, n and α. Note that no orientation with respect to x, y or z is assumed.

Table 3. Greek variables used in this paper and in Paper I.

Variable	Explanation	Reference
α	Semivertical angle of umbral and antumbral cones	equation (10) and Fig. 5
β	Auxiliary angle	equation (77)
$\beta^\vee$	Auxiliary angle	equation (78)
γ	Auxiliary angle	equation (81)
$\gamma^\vee$	Auxiliary angle	equation (82)
δ	Commonly-appearing auxiliary variable	equation (14)
Δ	Auxiliary variable	equation (151)
ϵ	Auxiliary angle	equation (79)
$\epsilon^\vee$	Auxiliary angle	equation (80)
ζ	Auxiliary angle	equation (159)
$\eta_{\rm sha}$	Angular diameter of shadow on primary as seen by observer on fourth body	equation (155)
η_{14}	Angular diameter of primary as seen by observer on fourth body	equation (164)
θ_{13}	Angular diameter of primary as seen by observer on target in penumbral shadow	Section B3 of Paper I
θ_{23}	Angular diameter of occulter as seen by observer on target in penumbral shadow	Section B3 of Paper I
ι	Auxiliary angle	equation (162)
κ	Angle between $\vec{r}$ and $\vec{r}_{13}$	equation (47)
$\nu_{\rm ant}^{\rm cen}$	Auxiliary angle	equation (86)
$\nu_{\rm ant}^{\rm edge}$	Auxiliary angle	equation (85)
$\nu_{\rm umb}^{\rm cen}$	Auxiliary angle	equation (84)
$\nu_{\rm umb}^{\rm edge}$	Auxiliary angle	equation (83)
ξ	Angle between $\vec{r}$ and $\vec{r}_{12}$	equation (46)
Π	True anomaly	
σ	Longitude of point on target	Section 5.2
τ	Time of pericentre passage	
ϕ_{13}	Angular diameter of primary as seen by observer on target in umbral shadow	Section A4 of Paper I
ϕ_{23}	Angular diameter of occulter as seen by observer on target in umbral shadow	Section A4 of Paper I
χ	Auxiliary angle	equation (156)
ψ	Angle between $\vec{r}_{12}$ and $\vec{r}_{13}$	equation (56)
$\psi_\blacklozenge$	Value of ψ where target is tangent and external to the cone	equation (58)
$\psi_\diamond$	Value of ψ where target is tangent and internal to the cone	equation (59)
$\psi_\Updownarrow$	Value of ψ where target is tangent to the cone axis	Section 7.2
$\psi_{\rm loc}$	Angle between $\vec{r}_{12}$ and a specific point on target surface	equation (67)
ω	Auxiliary angle	equation (75)
$\omega^\vee$	Auxiliary angle	equation (76)
Ω	Longitude of ascending node	

axes coinciding with the z-axis ($x_{12} = y_{12} = 0, z_{12} = r_{12}$). In Paper I (equation A17), this reduced cone was also translated by a distance h, with an origin that was already translated by a distance n.

Here the vertex is translated along the cone's axis by a distance of $h + n$, where this sum is related to R_1, R_2 and r_{12} through Fig. 5 as

$$h + n = \frac{R_1 r_{12}}{R_1 - R_2} = \frac{R_1}{\delta}, \tag{13}$$

where

$$\delta \equiv \frac{R_1 - R_2}{r_{12}}. \tag{14}$$

δ is a particularly helpful auxiliary variable representing a fundamental ratio in eclipse geometry, and is used throughout the paper. In fact, by utilising δ throughout the paper, I will be able to convert all of my results from the antumbral case to the penumbral case quickly in Section 9.

Introducing the correct translation and rotation finally yields the equation of the cone:

$$\left(\frac{h^2}{h^2 + R_{\rm c}^2}\right)\left[\left(x - \frac{x_{12}\,(h+n)}{r_{12}}\right)^2 + \left(y - \frac{y_{12}\,(h+n)}{r_{12}}\right)^2 + \left(z - \frac{z_{12}\,(h+n)}{r_{12}}\right)^2\right] = \left[\frac{x_{12}}{r_{12}}\left(x - \frac{x_{12}\,(h+n)}{r_{12}}\right) + \frac{y_{12}}{r_{12}}\left(y - \frac{y_{12}\,(h+n)}{r_{12}}\right) + \frac{z_{12}}{r_{12}}\left(z - \frac{z_{12}\,(h+n)}{r_{12}}\right)\right]^2 \tag{15}$$

where

$$r_{12} = \sqrt{x_{12}^2 + y_{12}^2 + z_{12}^2}. \tag{16}$$

The coefficients of the resulting quadric for the cone's

Table 4. Other variables used in this paper and in Paper I.

Variable	Explanation	Reference
$\mathfrak{x}$	Component of transformed coordinate system	equation (42)
$\mathfrak{x}_{\rm offset}$	Offset from origin of transformed coordinate system	equation (44)
$\mathfrak{y}$	Component of transformed coordinate system	equation (43)
$\mathfrak{y}_{\rm offset}$	Offset from origin of transformed coordinate system	equation (45)
$\mathcal{C}$	Auxiliary variables	equations (126-129)
$\mathfrak{d}$	Duration of transit	equations (148)
$\mathfrak{D}$	Duration of ingress or egress only	equations (149)
$\mathfrak{e}$	End time for transit	equation (147)
$\mathfrak{f}$	Frequency of transits	equation (150)
$\mathcal{F}$	Auxiliary variable	equation (72)
$\mathcal{G}$	Auxiliary variable	equation (73)
$\mathcal{G}^{\vee}$	Auxiliary variable	equation (74)
$\mathfrak{G}$	Gravitational constant	equation (113)
$\mathfrak{l}$	Latitude for point on target	Section 5.2
$\mathcal{L}_{\rm ant}$	Antumbral shadow length	equations (71) and (111)
$\mathcal{L}^{\rm syz}_{\rm ant}$	Antumbral shadow length at syzygy $= 2R_{\rm ant}$	equation (94)
$\mathcal{L}_{\rm umb}$	Umbral shadow length	equations (70) and (110)
$\mathcal{L}^{\rm syz}_{\rm umb}$	Umbral shadow length at syzygy $= 2R_{\rm umb}$	equation (93)
$\mathcal{M}$	Mean anomaly	equation (112)
$\mathfrak{n}$	Mean motion	equation (113)
$\mathcal{P}$	Auxiliary variables	equations (130-131)
$\mathfrak{s}$	Start time for transit	equation (146)
$\mathcal{S}$	Auxiliary variables	equations (122-125)
$\mathfrak{u}$	Component in transformed coordinate system	Section 3.2
$\mathcal{U}$	Auxiliary variables	equations (132-133)
$\mathfrak{v}$	Component in transformed coordinate system	Section 3.2
$\mathfrak{w}$	Component in transformed coordinate system	Section 3.2

surface – which is infinite in two directions – can be expressed in the desired variables as

$$A_{\rm cone} = \frac{1}{r_{12}^2}\left[r_{12}^2 - x_{12}^2 - (R_1 - R_2)^2\right] = 1 - \delta^2 - \left(\frac{x_{12}}{r_{12}}\right)^2, \quad (17)$$

$$B_{\rm cone} = \frac{1}{r_{12}^2}\left[r_{12}^2 - y_{12}^2 - (R_1 - R_2)^2\right] = 1 - \delta^2 - \left(\frac{y_{12}}{r_{12}}\right)^2, \quad (18)$$

$$C_{\rm cone} = \frac{1}{r_{12}^2}\left[r_{12}^2 - z_{12}^2 - (R_1 - R_2)^2\right] = 1 - \delta^2 - \left(\frac{z_{12}}{r_{12}}\right)^2, \quad (19)$$

$$D_{\rm cone} = -\frac{x_{12}y_{12}}{r_{12}^2}, \quad (20)$$

$$E_{\rm cone} = -\frac{y_{12}z_{12}}{r_{12}^2}, \quad (21)$$

$$F_{\rm cone} = -\frac{x_{12}z_{12}}{r_{12}^2}, \quad (22)$$

$$G_{\rm cone} = \frac{R_1\left(R_1 - R_2\right)x_{12}}{r_{12}^2} = R_1\delta\left(\frac{x_{12}}{r_{12}}\right), \quad (23)$$

$$H_{\rm cone} = \frac{R_1\left(R_1 - R_2\right)y_{12}}{r_{12}^2} = R_1\delta\left(\frac{y_{12}}{r_{12}}\right), \quad (24)$$

$$J_{\rm cone} = \frac{R_1\left(R_1 - R_2\right)z_{12}}{r_{12}^2} = R_1\delta\left(\frac{z_{12}}{r_{12}}\right), \quad (25)$$

$$K_{\rm cone} = -R_1^2. \quad (26)$$

3.3 Cartesian equation of the intersection

Now I construct the equation of the shadow by combining the results of the equations for the cone and target. To do so I solve equation (8) for $x^2 + y^2 + z^2$ and substitute the expression into the quadric equation for the cone. The result is

$$A_{\rm int}x^2 + B_{\rm int}y^2 + C_{\rm int}z^2 + 2D_{\rm int}xy + 2E_{\rm int}yz + 2F_{\rm int}xz + 2G_{\rm int}x + 2H_{\rm int}y + 2J_{\rm int}z + K_{\rm int} = 0 \quad (27)$$

where "int" denotes intersection, and with

$$A_{\rm int} = \left(\frac{x_{12}}{r_{12}}\right)^2, \quad (28)$$

$$B_{\rm int} = \left(\frac{y_{12}}{r_{12}}\right)^2, \quad (29)$$

$$C_{\rm int} = \left(\frac{z_{12}}{r_{12}}\right)^2, \quad (30)$$

$$D_{\rm int} = \frac{x_{12}y_{12}}{r_{12}^2}, \quad (31)$$

$$E_{\rm int} = \frac{y_{12}z_{12}}{r_{12}^2}, \quad (32)$$

$$F_{\rm int} = \frac{x_{12}z_{12}}{r_{12}^2}, \quad (33)$$

$$G_{\rm int} = -x_{13}\left(1-\delta^2\right) - \frac{\delta R_1 x_{12}}{r_{12}}, \tag{34}$$

$$H_{\rm int} = -y_{13}\left(1-\delta^2\right) - \frac{\delta R_1 y_{12}}{r_{12}}, \tag{35}$$

$$J_{\rm int} = -z_{13}\left(1-\delta^2\right) - \frac{\delta R_1 z_{12}}{r_{12}}, \tag{36}$$

$$K_{\rm int} = R_1^2 + \left(1-\delta^2\right)\left(r_{13}^2 - R_3^2\right). \tag{37}$$

The surfaces of both the target and cone intersect only when there exist $\{x, y, z\}$ which satisfy equation (27).

4 SHAPE OF THE SHADOW

In order to determine the shape of the shadow, I utilise the properties of quadrics (Pgs. 316-319, Zwillinger 1996). He showed that the shape defined by the quadric is determined by the following quantities, all using the coefficients of the Cartesian equation of the intersection. The first quantity is

$$\text{Rank}\begin{vmatrix} A_{\rm int} & D_{\rm int} & F_{\rm int} \\ D_{\rm int} & B_{\rm int} & E_{\rm int} \\ F_{\rm int} & E_{\rm int} & C_{\rm int} \end{vmatrix} = 1. \tag{38}$$

and the next quantity is

$$\text{Rank}\begin{vmatrix} A_{\rm int} & D_{\rm int} & F_{\rm int} & G_{\rm int} \\ D_{\rm int} & B_{\rm int} & E_{\rm int} & H_{\rm int} \\ F_{\rm int} & E_{\rm int} & C_{\rm int} & J_{\rm int} \\ G_{\rm int} & H_{\rm int} & J_{\rm int} & K_{\rm int} \end{vmatrix} = 3. \tag{39}$$

These two values alone reveal that a *transit shadow is in the shape of a parabolic cylinder*. For a visual representation of this shape, see Fig. 4.

Another way of demonstrating the character of the shadow is by writing out and appropriately transforming equation (27). I note that the equation may be written as

$$R_1^2 r_{12}^2 + \left(x x_{12} + y y_{12} + z z_{12}\right)^2 - 2\delta R_1 r_{12}\left(x x_{12} + y y_{12} + z z_{12}\right) + \left(1-\delta^2\right) r_{12}^2\left[r_{13}^2 - R_3^2 - 2\left(x x_{13} + y y_{13} + z z_{13}\right)\right] = 0. \tag{40}$$

I can rewrite this equation in the standard form for a parabolic cylinder as

$$\left(\mathfrak{x} - \mathfrak{x}_{\rm offset}\right)^2 + 2\left(\mathfrak{y} - \mathfrak{y}_{\rm offset}\right) = 0, \tag{41}$$

by making the transformations

$$\mathfrak{x} \to x x_{12} + y y_{12} + z z_{12} \tag{42}$$

and

$$\mathfrak{y} \to -\left(x x_{13} + y y_{13} + z z_{13}\right) r_{12}^2\left(1-\delta^2\right), \tag{43}$$

where

$$\mathfrak{x}_{\rm offset} = \delta R_1 r_{12} \tag{44}$$

and

$$\mathfrak{y}_{\rm offset} = -\frac{1}{2}\left(1-\delta^2\right) r_{12}^2\left(r_{13}^2 + R_1^2 - R_3^2\right). \tag{45}$$

5 CONDITION TO BE "IN TRANSIT"

A natural follow-up to the last section is the determination of when a system would be in transit in the first place. "In transit" can refer to a target that is partially or fully enveloped within the radiation cone.

5.1 Shadow anywhere on target

The condition for these limiting cases may be derived from equation (40) by noting that the Cartesian-based expressions there can all be expressed as dot products.

5.1.1 Radial equation of the intersection

I define ξ as the angle between $\vec{r}$ and $\vec{r}_{12}$ and κ as the angle between $\vec{r}$ and $\vec{r}_{13}$. Then by assuming r is the distance to some point on the intersection,

$$\cos\xi = \frac{x x_{12} + y y_{12} + z z_{12}}{r r_{12}} \tag{46}$$

and

$$\cos\kappa = \frac{x x_{13} + y y_{13} + z z_{13}}{r r_{13}}. \tag{47}$$

The equation of the intersection hence becomes

$$r^2\cos^2\xi + R_1^2 - 2\delta r R_1\cos\xi - \left(1-\delta^2\right)\left(2 r r_{13}\cos\kappa - r_{13}^2 + R_3^2\right) = 0. \tag{48}$$

Solving for r yields

$$r = \frac{1}{\cos^2\xi}\Bigg[\delta R_1\cos\xi + r_{13}\cos\kappa\left(1-\delta^2\right) \pm\sqrt{1-\delta^2}\Bigg\{2\delta R_1 r_{13}\cos\xi\cos\kappa + \left(1-\delta^2\right) r_{13}^2\cos^2\kappa - \cos^2\xi\left(r_{13}^2 + R_1^2 - R_3^2\right)\Bigg\}^{1/2}\Bigg]. \tag{49}$$

For a given ξ and κ, the two signs in equation (49) refer to intersections occurring on the near side (negative sign) and far side (positive sign) of the target.

5.1.2 Target tangent to cone

Equation (49) accounts for all possible values of r. These would, for example, trace out the entire mesh in Fig. 4. My concern here is to determine the conditions for the target to be tangent to the cone, which will allow me to derive a transit criterion for snapshots and other quantities when I introduce motion. If the target is tangent to the cone, then r can take one value only, denoted by $r_{\rm tan}$, requiring the determinant of equation (49) to be zero[2]. This requirement yields

[2] I also consider only positive values of $\cos\xi$ and $\cos\kappa$. The negative values would correspond to the target intersecting the cone "behind" the primary, as the cone extends infinitely in both directions. In exoplanetary science, this intersection would be referred to as a *secondary transit.* An analytical treatment of secondary transits may be carried out by proceeding with the analysis in this section by assuming $\cos\kappa < 0$. This analysis may eventu-

$$\cos\kappa_{\rm tan} = \cos\xi_{\rm tan}\left[\frac{\sqrt{(r_{13}^2 - R_3^2)(1-\delta^2) + R_1^2} - \delta R_1}{r_{13}(1-\delta^2)}\right] \quad (50)$$

and

$$r_{\rm tan} = \frac{\sqrt{(1-\delta^2)(r_{13}^2 - R_3^2) + R_1^2}}{\cos\xi_{\rm tan}}. \quad (51)$$

In order to solve simultaneously for $r_{\rm tan}$, $\cos\xi_{\rm tan}$ and $\cos\kappa_{\rm tan}$ in terms of given variables, I need one more equation: I use a relation which is obtained by the triangle which connects the target (here tangent to the cone) and the centre of the primary:

$$R_3^2 = r_{\rm tan}^2 + r_{13}^2 - 2r_{\rm tan}r_{13}\cos\kappa_{\rm tan}. \quad (52)$$

The final result is

$$r_{\rm tan} = \sqrt{\frac{K_{\rm int} + R_1^2 - 2\delta R_1\sqrt{K_{\rm int}}}{1-\delta^2}}, \quad (53)$$

$$\cos\xi_{\rm tan} = \sqrt{\frac{K_{\rm int}(1-\delta^2)}{K_{\rm int} + R_1^2 - 2\delta R_1\sqrt{K_{\rm int}}}} = \frac{\sqrt{K_{\rm int}}}{r_{\rm tan}}, \quad (54)$$

$$\cos\kappa_{\rm tan} = \frac{K_{\rm int}^{3/2} - \delta R_1 K_{\rm int}}{r_{13}\sqrt{(1-\delta^2)K_{\rm int}\left[K_{\rm int} + R_1^2 - 2\delta R_1\sqrt{K_{\rm int}}\right]}}. \quad (55)$$

In order to develop an explicit criterion for transits, I wish to obtain a functional form in terms of the distance vectors to the centres of the occulter and target (not the distance to the shadow itself). So let ψ represent the angle between $\vec{r}_{12}$ and $\vec{r}_{13}$ such that

$$\cos\psi = \frac{x_{12}x_{13} + y_{12}y_{13} + z_{12}z_{13}}{r_{12}r_{13}}. \quad (56)$$

The angle ψ also represents a crucial way to reduce the number of degrees of freedom in the geometry, and will be applied repeatedly throughout the paper.

Denote the limiting values of ψ which correspond to when the target is *tangent but external* to the cone as $\psi_{\blacklozenge}$: it is at these locations where the ingress begins and the egress ends. The criterion for a target to be in transit is then:

$$\cos\psi \geqslant \cos\psi_{\blacklozenge}, \quad (57)$$

where

$$|\psi_{\blacklozenge}| = |\xi_{\rm tan}| + |\kappa_{\rm tan}|, \quad (58)$$

which provides the basis for many further results in this paper. The case where the target is *tangent but internal* to the cone is also of interest, for determining if, when and where the target is fully engulfed in the shadow. Denote this critical angle as $\psi_{\diamond}$, and note that $\cos\psi_{\diamond} \geqslant \cos\psi_{\blacklozenge}$. Then

$$|\psi_{\diamond}| = |\xi_{\rm tan} - \kappa_{\rm tan}|. \quad (59)$$

These tangent cases are illustrated graphically in Fig. 6.

ally yield, for example, an analytical expression for the relative durations of the primary and secondary transits.

5.1.3 Full engulfment in the shadow

The figure demonstrates that a target which is tangent but internal to the cone is not necessarily engulfed in shadow. The condition for the target to be fully engulfed in the shadow is

$$\cos\psi \geqslant \cos\psi_{\diamond} \quad \& \quad |\xi_{\rm tan}| \geqslant |\kappa_{\rm tan}|. \quad (60)$$

5.1.4 Special case of syzygy

I can perform a check by considering the critical target radius for engulfment in the special case of syzygy. Here, $\xi_{\rm tan} = \kappa_{\rm tan}$, which yields, for the umbral and antumbral cases respectively,

$$R_3^{\dagger} = R_1 - r_{13}\delta, \quad (61)$$

$$R_3^{\ddagger} = r_{13}\delta - R_1. \quad (62)$$

These equations are equivalent to those of Eqs. A12-A13 of Paper I. Note also that a target whose centre lies at the vertex of the radiation cone can never be engulfed in shadow. This special case corresponds to $R_1 = r_{13}\delta$.

The physical meaning of the similar scenario where an observer on the target coincides with the cone's vertex is the following: the angular diameter of the occulter asymptotically would cover the primary's disc such that the eclipse would be considered just barely total. The size of the umbral shadow on the target would be asymptotically zero at the observer's location. Other locations on the surface which are in shadow must be covered in the antumbral shadow.

5.2 Shadow on specific location on target

The last paragraph illustrates the potential usefulness of a transit criterion for a specific point $(x_{\rm loc}, y_{\rm loc}, z_{\rm loc})$ on the target's surface. In this section, I explore this scenario.

Assume that the point has a specific latitude $\mathfrak{l}$ and longitude σ, and consider this point to be infinitesimal. Its Cartesian location is (Pg. 205 of Roy 2005)

$$x_{\rm loc} = x_{13} - R_3\cos\sigma\cos\mathfrak{l}, \quad (63)$$

$$y_{\rm loc} = y_{13} - R_3\sin\sigma\cos\mathfrak{l}, \quad (64)$$

$$z_{\rm loc} = z_{13} - R_3\sin\mathfrak{l}. \quad (65)$$

Then by assuming that this point is chosen to be on the near side of the target, I can treat the point as representing the new target with infinitesimal radius. Hence, the condition to be in transit is

$$\cos\psi_{\rm loc} \geqslant \cos\left[\psi_{\blacklozenge}(R_3 = 0, r_{13} \to r_{\rm loc})\right], \quad (66)$$

where

$$\cos\psi_{\rm loc} \equiv \frac{x_{12}x_{\rm loc} + y_{12}y_{\rm loc} + z_{12}z_{\rm loc}}{r_{12}r_{\rm loc}} \quad (67)$$

and

$$r_{\rm loc} = \sqrt{x_{\rm loc}^2 + y_{\rm loc}^2 + z_{\rm loc}^2}. \quad (68)$$

Note that because this location is an infinitesimal point, it can never be partially engulfed in a shadow.

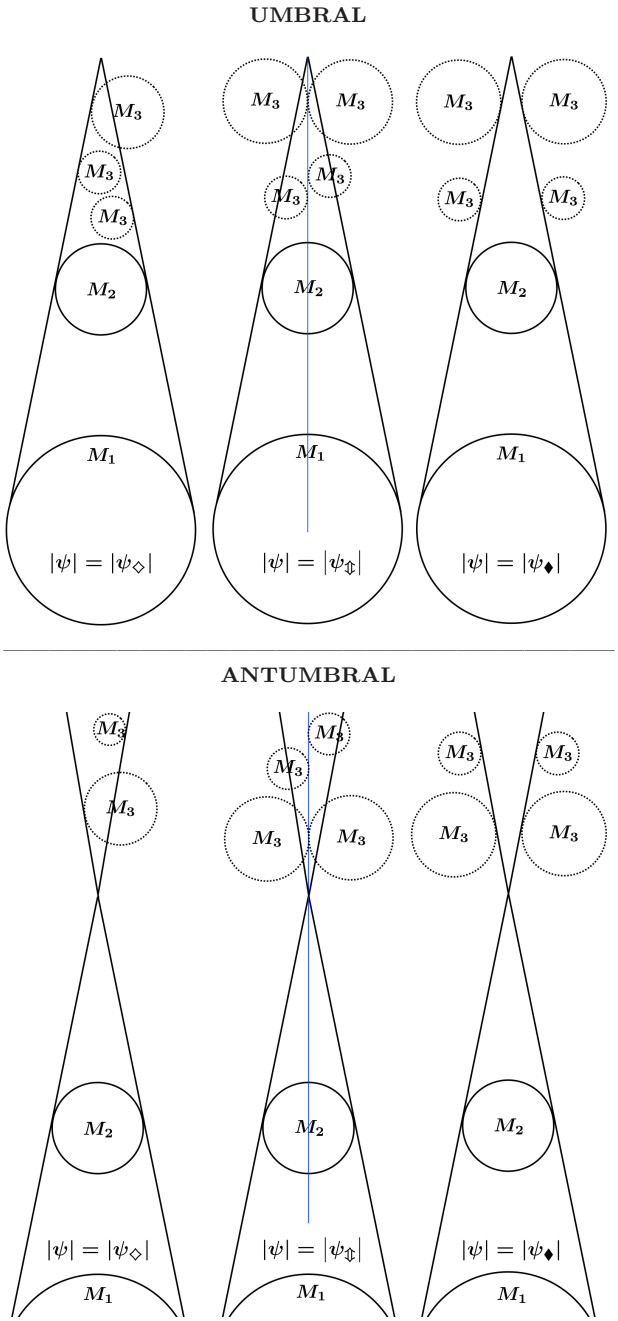

Figure 6. The geometric meaning of the critical angle values of $\psi_\diamond$, $\psi_\blacklozenge$, and $\psi_\Updownarrow$ for both umbral cases (top panels) and antumbral cases (bottom panels). Some different possible locations of the target are illustrated with dotted M_3 spheres.

6 TOTAL VS. ANNULAR ECLIPSE CRITERION

In the last section, I determined the conditions necessary for a transit to exist. Supposing it does, now I determine whether the transit produces a total or annular eclipse. This exercise involves determining which nappe intersects the near side of the target at a given moment in time. In rare cases, throughout a transit, the target's near side could at different times intersect both nappes, yielding a mixed or hybrid eclipse (here I consider just a snapshot in time).

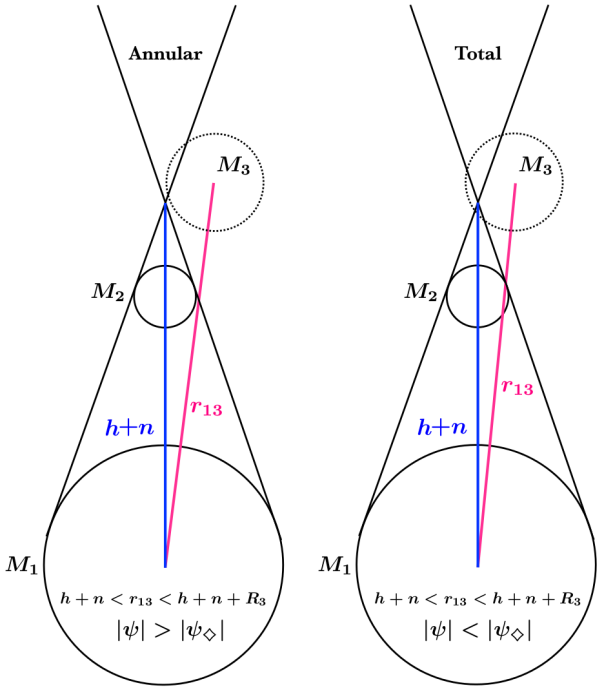

Figure 7. Determining whether an eclipse is total or annular. The figure illustrates the two cases when $h+n < r_{13} < h+n+R_3$.

For perspective, the criterion for an annular eclipse to occur at syzygy (equation A7 of Paper I) is $r_{13} \geqslant h+n+R_3$, which was derived by placing the target just above the cone's vertex at syzygy. The criterion for a total eclipse to occur was obtained simply by switching the sign.

Here, in the off-syzygy cases, there is a subtle difference. The same criterion for an annular eclipse still holds, but is sufficient, not necessary. For a total eclipse to occur, a sufficient but not necessary condition is $r_{13} < h+n$, because I consider only the near side of the target. Otherwise, when $h+n < r_{13} < h+n+R_3$, the type of eclipse depends on ψ. Fig. 7 illustrates both possibilities: when $|\psi| > |\psi_\diamond|$, the eclipse is annular. Overall then,

$$\begin{aligned} &r_{13} \geqslant h+n+R_3, && && \text{annular} \\ &h+n < r_{13} < h+n+R_3 \quad \& \quad |\psi| \geqslant |\psi_\diamond|\,, && && \text{annular} \\ &h+n < r_{13} < h+n+R_3 \quad \& \quad |\psi| < |\psi_\diamond|\,, && && \text{total} \\ &r_{13} \leqslant h+n, && && \text{total.} \end{aligned} \tag{69}$$

I emphasise that this criterion applies only when the system is in transit in the first place (equation 57). In Table 5, I summarise some important criteria so far listed.

At syzygy, $\psi = 0$, and hence $|\psi| < |\psi_\diamond|$ is always true. Therefore, in this case, the criterion from Paper I is recovered.

7 SIZE OF SHADOW

Now I pursue the task of determining the size of the shadow when the target intersects the surface of the radiation cone, using only the given variables $\{R_1, R_2, R_3, \vec{r}_{12}, \vec{r}_{13}\}$. To do so, I appeal to brute-force geometry from Figs. 8-18, which

Table 5. Summary of some important criteria

Criteria		Meaning
$\cos\psi < \cos\psi_{\blacklozenge}$		Not in transit
$\cos\psi \geqslant \cos\psi_{\blacklozenge}$:		In transit
	$\cos\psi \geqslant \cos\psi_{\diamond}$ & $\lvert\xi_{\tan}\rvert \geqslant \lvert\kappa_{\tan}\rvert$	Engulfed in shadow
	$r_{13} \geqslant h+n+R_3$	Annular eclipse
	$h+n<r_{13}<h+n+R_3$ & $\lvert\psi\rvert \geqslant \lvert\psi_{\diamond}\rvert$	Annular eclipse
	$h+n<r_{13}<h+n+R_3$ & $\lvert\psi\rvert < \lvert\psi_{\diamond}\rvert$	Total eclipse
	$r_{13} \leqslant h+n$	Total eclipse
	$\cos\psi = 1$	Syzygy

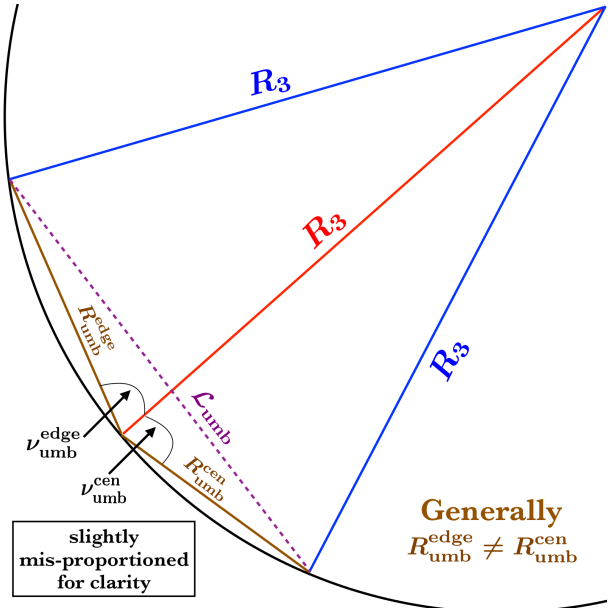

Figure 8. Defining the size of a shadow, with $\mathcal{L}$. The endpoints of the dashed purple lines represent locations where the radiation cone intersects the shown target for both umbral and antumbral cases (the "umb" subscripts shown here are just for demonstration purposes, but could equally read "ant").

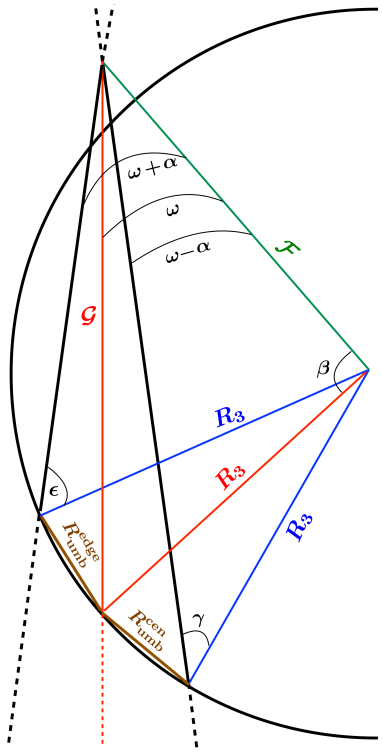

Figure 9. Geometry for determining size of an umbral shadow for simultaneous ingress and egress. Shown is the target, with the radiation cone bounded by diagonal black lines.

cover both the umbral and antumbral cases; the end result for each case is a single, compact piecewise function.

First, in Section 7.1, I consider the general case of the target being in both ingress and egress (see Fig. 3), like the Earth is during nearly all of an annular or total eclipse of the Sun and Moon. Then in Section 7.2 I look at the geometry of ingress only or egress only. In Section 7.3 I consider the case where the entire target is engulfed, before collating the results in Section 7.4.

7.1 Simultaneous ingress and egress

7.1.1 Size definition

The shape and size of the shadow can vary considerably and non-monotonically during a transit, even under the assumption of a spherical target. Consequently, I seek a simple measure to quantify its size, and denote the projected lengths $\mathcal{L}_{\rm umb}$ and $\mathcal{L}_{\rm ant}$ as the shadow "sizes" for the umbral and antumbral cases. For simultaneous ingress and egress, these lengths are split into two usually unequal projected radii of the shadow ($R^{\rm edge}_{\rm umb}$ and $R^{\rm cen}_{\rm umb}$ for the umbral case and $R^{\rm edge}_{\rm ant}$

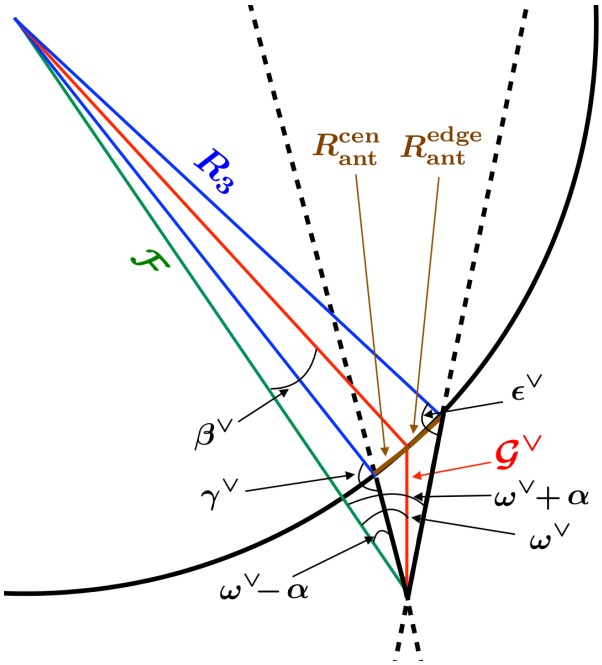

Figure 10. Geometry for determining size of an antumbral shadow for simultaneous ingress and egress. Shown is the target, with the radiation cone bounded by diagonal black lines.

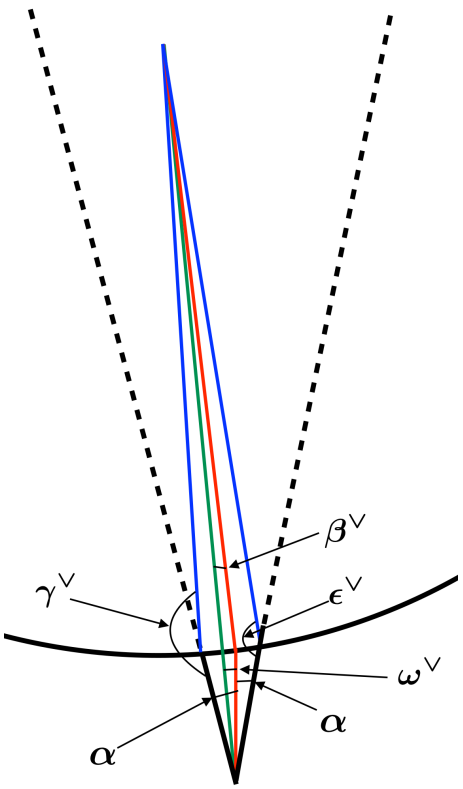

Figure 11. Geometry for determining size of an antumbral shadow for geometries closer to syzygy than grazing. Despite the difference in relative location of $\mathcal{F}$ (the green line) as compared to Fig. 10, the relevant geometric quantities in the main text remain unchanged.

and $R_{\rm ant}^{\rm cen}$ for the antumbral case) as in Fig 8. Hence, through the law of cosines,

$$\mathcal{L}_{\rm umb} = \sqrt{\left(R_{\rm umb}^{\rm edge}\right)^2 + (R_{\rm umb}^{\rm cen})^2 - 2R_{\rm umb}^{\rm edge}R_{\rm umb}^{\rm cen}\cos\left(\nu_{\rm umb}^{\rm edge} + \nu_{\rm umb}^{\rm cen}\right)}, \tag{70}$$

$$\mathcal{L}_{\rm ant} = \sqrt{\left(R_{\rm ant}^{\rm edge}\right)^2 + (R_{\rm ant}^{\rm cen})^2 - 2R_{\rm ant}^{\rm edge}R_{\rm ant}^{\rm cen}\cos\left(\nu_{\rm ant}^{\rm edge} + \nu_{\rm ant}^{\rm cen}\right)}. \tag{71}$$

I now set about determining all of the quantities on the right-hand-sides of equations (70)-(71).

7.1.2 Auxiliary variables

First consider Figs. 9-11, which cover the umbral and antumbral cases in a general fashion. The auxiliary variable $\mathcal{F}$ is common to both cases, and is the distance from the cone's vertex to the target centre:

$$\begin{aligned}\mathcal{F} &= \left[\left(x_{13} - \frac{x_{12}\,(h+n)}{r_{12}}\right)^2 \right.\\ &\quad \left. + \left(y_{13} - \frac{y_{12}\,(h+n)}{r_{12}}\right)^2 + \left(z_{13} - \frac{z_{12}\,(h+n)}{r_{12}}\right)^2\right]^{1/2}\\ &= \sqrt{r_{13}^2 + \frac{R_1^2}{\delta^2} - \frac{2R_1 r_{13}}{\delta}\cos\psi}.\end{aligned} \tag{72}$$

The other variables are not common to both the umbral and antumbral cases. All of the differences in the umbral and antumbral cases stem from the relative location of the radiation cone's vertex to the near side of the target, which is manifested through the lengths $\mathcal{G}$ and $\mathcal{G}^\vee$:

$$\begin{aligned}\mathcal{G} &= h + n - \left(r_{13}\cos\psi - \sqrt{R_3^2 - r_{13}^2\sin\psi}\right)\\ &= \frac{R_1}{\delta} - \left(r_{13}\cos\psi - \sqrt{R_3^2 - r_{13}^2\sin\psi}\right),\end{aligned} \tag{73}$$

$$\begin{aligned}\mathcal{G}^\vee &= \left(r_{13}\cos\psi + \sqrt{R_3^2 - r_{13}^2\sin\psi}\right) - (h+n)\\ &= \left(r_{13}\cos\psi + \sqrt{R_3^2 - r_{13}^2\sin\psi}\right) - \frac{R_1}{\delta},\end{aligned} \tag{74}$$

and ω and $\omega^\vee$:

$$\omega = \arccos\left[\frac{\mathcal{F}^2 + \left(\frac{R_1}{\delta}\right)^2 - r_{13}^2}{2\mathcal{F}\left(\frac{R_1}{\delta}\right)}\right], \tag{75}$$

$$\omega^\vee = \pi - \omega. \tag{76}$$

The lengths G and $G^\vee$ are derived by applying the law of cosines to the triangle involving R_3, r_{13}, and the length from the origin to the near side of the target along the cone's axis. The correct sign in front of the square root is obtained by choosing either the near or far side of the target. For the

derivation of ω and $\omega^{\vee}$, I use the law of cosines rather than the law of sines. I do so in order to avoid a dependence on G and $G^{\vee}$, because when $R_3 \leqslant r_{13} \sin\psi$, then G and $G^{\vee}$ will not exist.

Various angles now follow. The choice of whether to apply the law of cosines or sines in the following depends on the quadrants in which these angles lie and in the interest of avoiding ambiguity:

$$\beta = \arccos\left[\frac{\mathcal{F}^2 + R_3^2 - \mathcal{G}^2}{2\mathcal{F}R_3}\right], \tag{77}$$

$$\beta^{\vee} = \arccos\left[\frac{\mathcal{F}^2 + R_3^2 - (\mathcal{G}^{\vee})^2}{2\mathcal{F}R_3}\right], \tag{78}$$

$$\epsilon = \arcsin\left[\frac{\mathcal{F}}{R_3}\sin\left(\omega + \alpha\right)\right], \tag{79}$$

$$\epsilon^{\vee} = \pi - \arcsin\left[\frac{\mathcal{F}}{R_3}\sin\left(\omega^{\vee} + \alpha\right)\right], \tag{80}$$

$$\gamma = \arcsin\left[\frac{\mathcal{F}}{R_3}\sin\left(\omega - \alpha\right)\right], \tag{81}$$

$$\gamma^{\vee} = \pi - \arcsin\left[\frac{\mathcal{F}}{R_3}\sin\left(\omega^{\vee} - \alpha\right)\right]. \tag{82}$$

Recall that α is the opening angle of the cone from equation (10) and Fig. 5, and is independent of the target.

For the umbral case, β can lie in the first or second quadrants, and ϵ and γ always lie within the first quadrant. However, for the antumbral case, although $\beta^{\vee}$ always lies within the first quadrant, $\epsilon^{\vee}$ always lies within the second quadrant, and $\gamma^{\vee}$ can lie in either the second quadrant (Fig. 10) or third quadrant (Fig. 11).

7.1.3 Final solution

I can now derive expressions for $R^{\rm edge}_{\rm umb}$, $R^{\rm cen}_{\rm umb}$, $R^{\rm edge}_{\rm ant}$, $R^{\rm cen}_{\rm ant}$ and the correspondingly labelled expressions for ν through the isosceles triangles formed by these variables (Fig. 8). I obtain

$$\nu^{\rm edge}_{\rm umb} = \pi - \frac{(\beta + \epsilon + \omega + \alpha)}{2}, \tag{83}$$

$$\nu^{\rm cen}_{\rm umb} = \frac{\beta + \gamma + \omega - \alpha}{2}, \tag{84}$$

$$\nu^{\rm edge}_{\rm ant} = \frac{\beta^{\vee} + \epsilon^{\vee} + \omega^{\vee} + \alpha}{2}, \tag{85}$$

$$\nu^{\rm cen}_{\rm ant} = \pi - \frac{(\beta^{\vee} + \gamma^{\vee} + \omega^{\vee} - \alpha)}{2}, \tag{86}$$

and, hence, through the law of sines,

$$R^{\rm edge}_{\rm umb} = R_3\frac{\sin\left[-\left(\beta + \epsilon + \omega + \alpha\right)\right]}{\sin\left[\nu^{\rm edge}_{\rm umb}\right]}$$

$$= -2R_3\cos\left[\frac{1}{2}\left(\alpha + \beta + \epsilon + \omega\right)\right], \tag{87}$$

$$R^{\rm cen}_{\rm umb} = R_3\frac{\sin\left[\beta + \gamma + \omega - \alpha\right]}{\sin\left[\nu^{\rm cen}_{\rm umb}\right]}$$

$$= 2R_3\cos\left[\frac{1}{2}\left(\alpha - \beta - \gamma - \omega\right)\right], \tag{88}$$

$$R^{\rm edge}_{\rm ant} = R_3\frac{\sin\left[\beta^{\vee} + \epsilon^{\vee} + \omega^{\vee} + \alpha\right]}{\sin\left[\nu^{\rm edge}_{\rm ant}\right]}$$

$$= 2R_3\cos\left[\frac{1}{2}\left(\alpha + \beta^{\vee} + \epsilon^{\vee} + \omega^{\vee}\right)\right], \tag{89}$$

$$R^{\rm cen}_{\rm ant} = R_3\frac{\sin\left[-\left(\beta^{\vee} + \gamma^{\vee} + \omega^{\vee} - \alpha\right)\right]}{\sin\left[\nu^{\rm cen}_{\rm ant}\right]}$$

$$= -2R_3\cos\left[\frac{1}{2}\left(\alpha - \beta^{\vee} - \gamma^{\vee} - \omega^{\vee}\right)\right]. \tag{90}$$

Inserting these expressions (equations 83-90) into equations (70) and (71) produces cancellations in β, $\beta^{\vee}$, ω, and $\omega^{\vee}$. Taking care to use the correct (physically realistic) root finally yields the following compact expressions

$$\mathcal{L}_{\rm umb} = 2R_3\sin\left[\alpha + \frac{\epsilon}{2} - \frac{\gamma}{2}\right], \tag{91}$$

$$\mathcal{L}_{\rm ant} = 2R_3\sin\left[-\left(\alpha + \frac{\epsilon^{\vee}}{2} - \frac{\gamma^{\vee}}{2}\right)\right]. \tag{92}$$

For the umbral shadow, when the target experiences both ingress and egress (see Fig. 3), the final answer is given by equation (91), which is solved by first computing variables in the following order from equations (11), (12), (10), (14), (72), (75), (79), and (81).

Similarly, for the antumbral shadow, the final answer is given by equation (92), which is solved by first computing variables in the following order from equations (11), (12), (10), (14), (72), (75), (76), (80), and (82).

7.1.4 At syzygy

I can check these solutions with those from the syzygy case, where $\psi = 0$ and hence $\mathcal{F} = |R_1 - \delta r_{13}|/\delta$. The value of subsequent auxiliary variables depends on whether R_1 is greater than δr_{13}.

Regardless, the umbral shadow size is given by

$$\mathcal{L}^{\rm syz}_{\rm umb} = 2R_3\sin\left\{\alpha - \arcsin\left[\frac{\left(r_{13} - \frac{R_1}{\delta}\right)\sin\alpha}{R_3}\right]\right\}. \tag{93}$$

This expression checks out because it is equivalent to twice the umbral syzygetic radius from equation (A19) of Paper I, just in a more compact form.

Now consider the antumbral syzygy. Here,

$$\mathcal{L}^{\rm syz}_{\rm ant} = 2R_3\sin\left\{-\alpha + \arcsin\left[\frac{\left(r_{13} - \frac{R_1}{\delta}\right)\sin\alpha}{R_3}\right]\right\}. \tag{94}$$

Similarly, this expression checks out because it is equivalent to twice the antumbral syzygetic radius from equation (A23) of Paper I.

7.1.5 Extreme shadow sizes

The shadow sizes range from zero when the target is tangent to the radiation cone, to a maximum value some time soon after the start of ingress, and then a local minimum at syzygy. Determining these quantities is facilitated by the compact forms of $\mathcal{L}_{\rm umb}$ and $\mathcal{L}_{\rm ant}$ from equations (91) and (92). They show that I need only consider the differences $(\epsilon - \gamma)$ and $(\epsilon^{\vee} - \gamma^{\vee})$ when determining the extremes.

By inspection, I see that when both ingress and egress

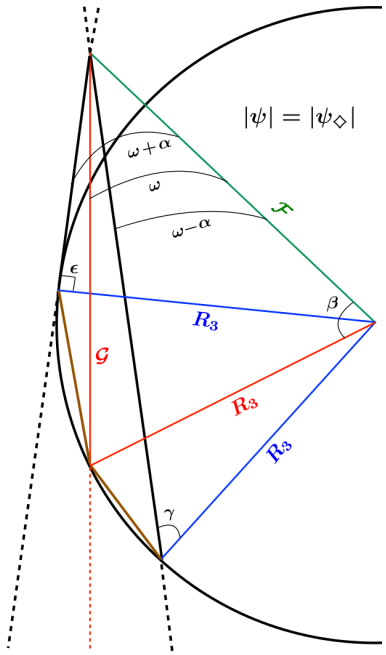

Figure 12. The configuration which gives the maximum size of the umbral shadow, where $\epsilon = \pi/2$.

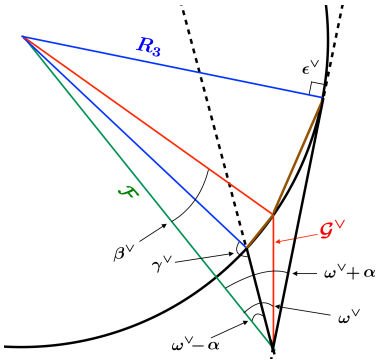

Figure 13. The configuration which gives the maximum size of the antumbral shadow, where $\epsilon^\vee = \pi/2$.

occur, the minimum value is achieved when $\epsilon = -\gamma$ and $\epsilon^\vee = -\gamma^\vee$, giving

$$\text{local min}\,(\mathcal{L}_{\rm umb}) = \mathcal{L}^{\rm syz}_{\rm umb}, \tag{95}$$

$$\text{local min}\,(\mathcal{L}_{\rm ant}) = \mathcal{L}^{\rm syz}_{\rm ant}. \tag{96}$$

In order to determine the maximum shadow size, consider the allowable range of ψ. The maximum value of ψ for which the target is in both ingress and egress occurs when $\epsilon = \pi/2$ or $\epsilon^\vee = \pi/2$, as in Figs. 12-13.

The value of ψ which corresponds to this situation is $\psi_\diamond$. The maximum shadow size must given by $\psi_\diamond$ because both that angle is the largest possible value of ψ and the size of the shadow scales positively with ψ, as shown by the functional dependence of $(\epsilon-\gamma)$ and $(\epsilon^\vee-\gamma^\vee)$ on ψ through $\mathcal{F}$, ω and $\omega^\vee$. Therefore,

$$\max\,(\mathcal{L}_{\rm umb}) = 2R_3 \sin\left[\alpha + \frac{\pi}{4} - \frac{\gamma\,(\psi=\psi_\diamond)}{2}\right], \tag{97}$$

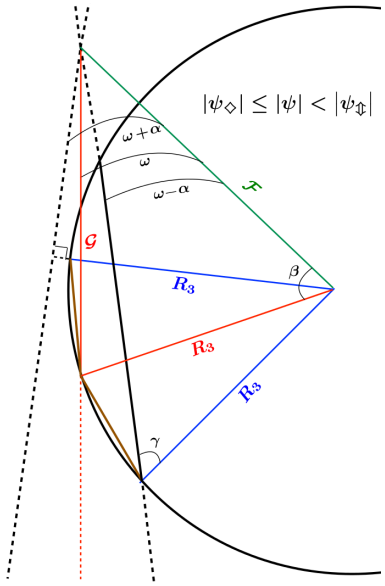

Figure 14. The umbral shadow during ingress only or egress only, when the cone axis still intersects the target.

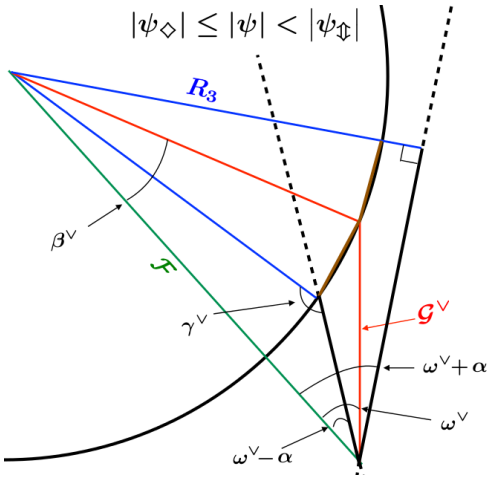

Figure 15. The antumbral shadow during ingress only or egress only, when the cone axis still intersects the target.

$$\max\,(\mathcal{L}_{\rm ant}) = 2R_3 \sin\left[-\left(\alpha + \frac{\pi}{4} - \frac{\gamma^\vee\,(\psi=\psi_\diamond)}{2}\right)\right]. \tag{98}$$

7.2 Ingress only or egress only

Now consider the case $|\psi_\diamond| \leqslant |\psi| < |\psi_\blacklozenge|$, when the target will still be in shadow and either ingress or egress will be occurring (but not both).

As $|\psi|$ increases from $|\psi_\diamond|$ to $|\psi_\blacklozenge|$, the shadow will decrease in size until disappearing at $\psi_\blacklozenge$. This transition comes in two parts, the first being $|\psi_\diamond| \leqslant |\psi| < |\psi_\Updownarrow|$ and the second being $|\psi_\Updownarrow| \leqslant |\psi| < |\psi_\blacklozenge|$, where $\psi_\Updownarrow$ is the value of ψ for which the target is tangent to the cone's axis (see Fig. 6).

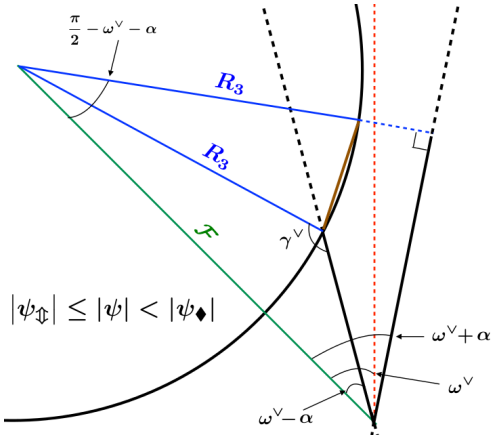

Figure 16. The antumbral shadow during ingress only or egress only, when the cone axis does not intersect the target.

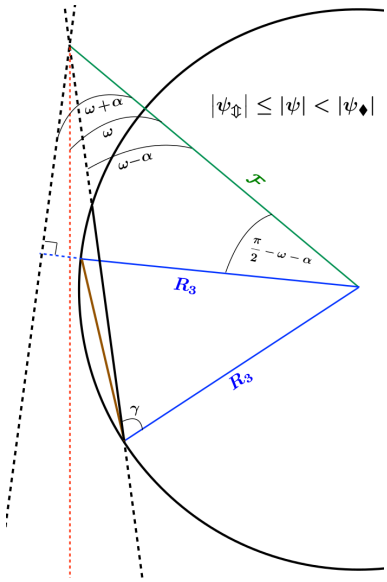

Figure 17. The umbral shadow during ingress only or egress only, when the cone axis does not intersect the target and when the far side of the target contains part of the cone surface-target intersection.

7.2.1 Cone axis intersecting target

This subsection describes the first part of this transition ($|\psi_\diamond| \leqslant |\psi| < |\psi_\Updownarrow|$), with geometries where the axis of the cone still intersects the target (see Figs. 14-15). In this case, $R^{\rm cen}_{\rm umb}$, $R^{\rm cen}_{\rm ant}$, $\nu^{\rm cen}_{\rm umb}$ and $\nu^{\rm cen}_{\rm ant}$ are computed in exactly the same way, as in equations (84), (86), (88) and (90). However, $R^{\rm edge}_{\rm umb}$ and $R^{\rm edge}_{\rm ant}$ are not, as now

$$R^{\rm edge}_{\rm umb} = -2R_3 \cos\left[\frac{1}{2}\left(\alpha+\beta+\frac{\pi}{2}+\omega\right)\right], \tag{99}$$

$$R^{\rm edge}_{\rm ant} = 2R_3 \cos\left[\frac{1}{2}\left(\alpha+\beta^\vee+\frac{\pi}{2}+\omega^\vee\right)\right]. \tag{100}$$

Consequently, for $\mathcal{L}_{\rm umb}$ and $\mathcal{L}_{\rm ant}$, equations (91-92) cannot be used. Instead equations (70-71) must be used, along with

$$\nu^{\rm edge}_{\rm umb} = \pi - \frac{\beta+\frac{\pi}{2}+\omega+\alpha}{2}, \tag{101}$$

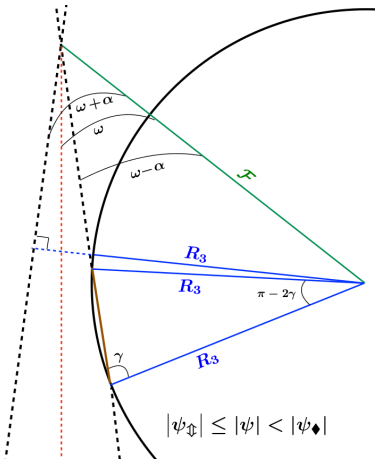

Figure 18. The umbral shadow during ingress only or egress only, when the cone axis does not intersect the target and when only the near side of the target contains part of the cone surface-target intersection.

$$\nu^{\rm edge}_{\rm ant} = \frac{\beta^\vee+\frac{\pi}{2}+\omega^\vee+\alpha}{2}. \tag{102}$$

Fortuitously, the final result is exactly the same as equations (91) and (92) but with $\epsilon = \epsilon^\vee = \pi/2$ such that

$$\mathcal{L}_{\rm umb} = 2R_3 \sin\left[\alpha+\frac{\pi}{4}-\frac{\gamma}{2}\right], \tag{103}$$

$$\mathcal{L}_{\rm ant} = 2R_3 \sin\left[-\left(\alpha+\frac{\pi}{4}-\frac{\gamma^\vee}{2}\right)\right]. \tag{104}$$

7.2.2 Cone axis not intersecting target

The next part of the transition, when the cone axis does not intersect the target (Figs. 16-18), occurs when

$$|\psi_\Updownarrow| \leqslant |\psi| < |\psi_\blacklozenge|\,. \tag{105}$$

Here,

$$R^{\rm edge}_{\rm umb} = R^{\rm edge}_{\rm ant} = 0, \tag{106}$$

and ω, $\omega^\vee$, γ and $\gamma^\vee$ are still defined.

For the antumbral case, the result is obtained from the geometry in Fig. 16, with another fortuitous result

$$\mathcal{L}_{\rm ant} = R^{\rm cen}_{\rm ant} = R_3 \frac{\sin\left[-\frac{\pi}{2}-2\alpha+\gamma^\vee\right]}{\sin\left[\frac{3\pi}{4}+\alpha-\frac{\gamma^\vee}{2}\right]}$$

$$= 2R_3 \sin\left[-\left(\alpha+\frac{\pi}{4}-\frac{\gamma^\vee}{2}\right)\right]. \tag{107}$$

Note that the shadow finally disappears when $\gamma^\vee/2-\alpha = \pi/4$, even though the radiation cone still intersects the target on the "far" side, which would not be illuminated anyway.

The umbral case, however, is trickier, because two subcases must be considered, as shown in Figs. 17 and 18. In Fig. 17, where the far side of the target is contained within the intersection, I obtain

$$\mathcal{L}_{\rm umb} = R^{\rm cen}_{\rm umb} = R_3 \frac{\sin\left[\frac{\pi}{2}+2\alpha-\gamma\right]}{\sin\left[\frac{\pi}{4}-\alpha+\frac{\gamma}{2}\right]} = 2R_3 \sin\left[\alpha+\frac{\pi}{4}-\frac{\alpha}{2}\right], \tag{108}$$

which is the same result as before (equation 103). However, in Fig. 18, where only the near side of the target is contained within the intersection, I have

$$\mathcal{L}_{\rm umb} = R_{\rm umb}^{\rm cen} = R_3 \frac{\sin\left[\pi - 2\gamma\right]}{\sin\left[\gamma\right]} = 2R_3 \cos\gamma \tag{109}$$

such that the shadow vanishes at $\gamma = \pi/2$. The transition point between the two subcases occurs when $\gamma = \pi/2 - 2\alpha$.

7.3 Engulfment in shadow

When the target is sufficiently small and distant (equation 60), the entire target may be engulfed. In this case, the size of the shadow may become ambiguous depending on one's definition of shadow. Paper I avoided this issue by not defining shadow surface areas at syzygy. My definition of shadow size here provides a convenient solution. The maximum possible value of both $\max\left(\mathcal{L}_{\rm umb}\right)$ and $\max\left(\mathcal{L}_{\rm ant}\right)$ (equations 97-98) is $2R_3$, when for the umbra $\gamma = 2\alpha - \pi/2$ and for the antumbra $\gamma = 2\alpha + 3\pi/2$.

7.4 Summary

All of the cases in this section can be compressed into the following final expressions for the umbra

$$\begin{aligned}
\mathcal{L}_{\rm umb} &= 2R_3, && |\psi| < |\psi_\diamond| \\
&&& \quad \& \quad |\xi_{\rm tan}| \geqslant |\kappa_{\rm tan}| \\
&= 2R_3 \sin\left[\alpha + \frac{\epsilon}{2} - \frac{\gamma}{2}\right], && |\psi| < |\psi_\diamond| \\
&&& \quad \& \quad |\xi_{\rm tan}| < |\kappa_{\rm tan}| \\
&= 2R_3 \sin\left[\alpha + \frac{\pi}{4} - \frac{\gamma}{2}\right], && |\psi_\diamond| \leqslant |\psi| < |\psi_\blacklozenge| \\
&&& \quad \& \quad \gamma < \frac{\pi}{2} - 2\alpha \\
&= 2R_3 \cos\gamma, && |\psi_\diamond| \leqslant |\psi| < |\psi_\blacklozenge| \\
&&& \quad \& \quad \gamma \geqslant \frac{\pi}{2} - 2\alpha \\
&= 0, && |\psi| \geqslant |\psi_\blacklozenge|\,,
\end{aligned} \tag{110}$$

and for the antumbra

$$\begin{aligned}
\mathcal{L}_{\rm ant} &= 2R_3, && |\psi| < |\psi_\diamond| \\
&&& \quad \& \quad |\xi_{\rm tan}| \geqslant |\kappa_{\rm tan}| \\
&= 2R_3 \sin\left[-\left(\alpha + \frac{\epsilon^\vee}{2} - \frac{\gamma^\vee}{2}\right)\right], && |\psi| < |\psi_\diamond| \\
&&& \quad \& \quad |\xi_{\rm tan}| < |\kappa_{\rm tan}| \\
&= 2R_3 \sin\left[-\left(\alpha + \frac{\pi}{4} - \frac{\gamma^\vee}{2}\right)\right], && |\psi_\diamond| \leqslant |\psi| < |\psi_\blacklozenge| \\
&= 0, && |\psi| \geqslant |\psi_\blacklozenge|\,.
\end{aligned} \tag{111}$$

which are all independent of $\psi_\Updownarrow$, $\mathcal{G}$, $\mathcal{G}^\vee$, β, and $\beta^\vee$.

8 TIME VARIATION

In Sections 3-7, I have characterised transits at specific snapshots in time. Now, I remove that restriction, and consider the evolution of bodies moving along fixed orbits, as described in Section 2.2. This assumption removes the three-body considerations of stability and transit timing variations, which have both become substantial research fields by themselves; in Appendix B I quantify the goodness of this approximation for a few cases. Nevertheless, as shown below, even the assumption of fixed orbits is not sufficiently simple to provide explicit analytical results in nearly all cases.

I assume that the masses and radii of the primary, occulter and target are all known, as well as some of their orbital parameters, depending on the specific case considered. Table 6 provides a list of the orbital parameters assumed for each case.

My goal is to determine eclipse frequencies and durations for various geometries. My procedure is to (i) find $(x_{12}, y_{12}, z_{12}, x_{13}, y_{13}, z_{13})$ in terms of the given orbital elements (Table 6) and time (equations 1-6), (ii) then compute $\psi(t)$ from equation (56), and (iii) finally compare $\psi(t)$ to $\psi_\blacklozenge(t)$ (equation 57) and $\psi_\diamond(t)$ (equation 60). The complexity of the time dependence determines the ability to carry out these tasks. The first task is completed in Appendix A, and the second task is completed in this section. The third task yields an explicit solution only in a special case, which is also presented in this section.

I perform these tasks in 12 different scenarios split according to whether the orbits are arbitrarily eccentric and coplanar (Section 8.1), circular and arbitrarily inclined (Section 8.2), or circular and coplanar (Section 8.3). Each of these scenarios are respectively denoted by the superscripts of (e), (i) and (cc).

I split each of these subsections into four cases of interest. These cases are: (a) One Star, Two Planets (1S2P)[3], (b) Two Stars, One Planet (2S1P) – where the planet is assumed to be a circumbinary planet – (c) One Star, One Planet, One Moon – Moon occulter (1M-MO), and (d) One Star, One Planet, One Moon – Planet occulter (1M-PO). I will use these abbreviations throughout the section for clarity. This split is useful because each of these scenarios typically utilise different initial conditions, as described in Section 2.1 and Table 6.

These scenarios also represent known or suspected planetary systems. The 1S2P case is particularly common. In fact, roughly 500 known planets reside in 1S2P systems (from the Exoplanet Orbit Database, at exoplanets.org, as of October 2018). A couple dozen planets reside in 2S1P systems, including, for example, PSR B1620-26, which features a planet orbiting both a millisecond pulsar and a white dwarf (Sigurdsson 1993; Thorsett et al. 1993; Sigurdsson et al. 2003), and Kepler-16, which features a planet orbiting both a K-type star and an M-type star (Doyle et al. 2011). The 1M-MO and 1M-PO cases can be represented, for example, by the Sun, Earth and Moon, when neglecting everything else in the solar system. In exoplanetary systems, no exomoon has yet been confirmed, although Teachey & Kipping

[3] This case is also equivalent to two moons orbiting a sufficiently luminous planet, such as Phobos and Deimos orbiting Mars (when all other solar system bodies are ignored).

Table 6. Orbital elements which are assumed to be given for the various cases in Section 8 and Appendix A: 1S2P = One Star, Two Planets; 2S1P = Two Stars, One Planet; 1M-MO = One Moon, One Planet, One Star, Moon occulter; 1M-PO = One Moon, One Planet, One Star, Planet occulter. The radii and masses of the primary, occulter and target are always assumed to be given.

Restrictions	1S2P	2S1P	1M-MO	1M-PO
Arbitrarily eccentric coplanar	a_{12}, a_{13}, e_{12}, e_{13}, Π_{12}, Π_{13}, τ_{12}, τ_{13}	a_{12}, a_{123}, e_{12}, e_{123}, Π_{12}, Π_{123}, τ_{12}, τ_{123}	a_{23}, a_{13}, e_{23}, e_{13}, Π_{23}, Π_{13}, τ_{23}, τ_{13}	a_{12}, a_{23}, e_{12}, e_{23}, Π_{12}, Π_{23}, τ_{12}, τ_{23}
Circular, arbitrarily inclined	a_{12}, a_{13}, i_{12}, i_{13}, Ω_{12}, Ω_{13}, w_{12}, w_{13}, τ_{12}, τ_{13}	a_{12}, a_{123}, i_{12}, i_{123}, Ω_{12}, Ω_{123}, w_{12}, w_{123}, τ_{12}, τ_{123}	a_{23}, a_{13}, i_{23}, i_{13}, Ω_{23}, Ω_{13}, w_{23}, w_{13}, τ_{23}, τ_{13}	a_{12}, a_{23}, i_{12}, i_{23}, Ω_{12}, Ω_{23}, w_{12}, w_{23}, τ_{12}, τ_{23}
Circular, coplanar	a_{12}, a_{13}, τ_{12}, τ_{13}	a_{12}, a_{123}, τ_{12}, τ_{123}	a_{23}, a_{13}, τ_{23}, τ_{13}	a_{12}, a_{23}, τ_{12}, τ_{23}

(2018) presented tantalizing evidence for one in the Kepler-1625 system. The discovery of exomoons will likely motivate additional eclipse studies.

8.1 Key parameters

The key parameter in this section, time (t), is propagated through the mean anomaly, $\mathcal{M}$, explicitly as follows:

$$\mathcal{M} = \mathfrak{n}\,(t-\tau)\,. \tag{112}$$

The variable τ is the time of pericentre passage, a crucial parameter for determinations of transit times. The proportionality constant is the mean motion, $\mathfrak{n}$, which is a function of only masses[4] and semimajor axis:

$$\mathfrak{n} = \sqrt{\frac{\mathfrak{G}\,(M_{\rm orbited}+M_{\rm orbiter})}{a^3}}, \tag{113}$$

where $\mathfrak{G}$ is the gravitational constant.

However, as demonstrated by equations (3-6), positions along an orbit are not generally given explicitly through the mean anomaly $\mathcal{M}$, but rather the true anomaly Π. These anomalies are related through Kepler's equation as

$$\mathcal{M} = \arctan\left[\frac{\sqrt{1-e^2}\sin\Pi}{e+\cos\Pi}\right] - \frac{e\sqrt{1-e^2}\sin\Pi}{1+e\cos\Pi}, \tag{114}$$

which is an implicit equation for Π in terms of $\mathcal{M}$. The result is that the comparison of ψ to $\psi_{\blacklozenge}$ and $\psi_{\diamond}$ are treated differently in the three subsections below:

- For eccentric and coplanar orbits (Section 8.2), ψ, $\psi_{\blacklozenge}$ and $\psi_{\diamond}$ are all functions of true anomaly, and hence comparisons at each moment in time throughout the orbits require an implicit solution for time through Kepler's equation;
- For inclined and circular orbits (Section 8.3), $\Pi = \mathcal{M} = \mathfrak{n}\,(t-\tau)$. Therefore, $\psi_{\blacklozenge}$ and $\psi_{\diamond}$ are no longer functions of true anomaly and instead are explicit functions of time (through δ and $K_{\rm int}$), and ψ is a different explicit function of time, depending on architecture. Hence Kepler's equation need not be solved, and the resulting relations require just a single implicit solution for time.
- For circular and coplanar orbits (Section 8.4), $\Pi = \mathcal{M} = \mathfrak{n}\,(t-\tau)$, and the situation is the same for inclined, circular orbits with one exception: For the 2P1S case, $\psi_{\blacklozenge}$ and $\psi_{\diamond}$ are constants, enabling explicit solutions for time.

[4] If all of the masses are not known, then one may neglect $M_{\rm orbiter}$ in the computation of $\mathfrak{n}$ with a corresponding loss of accuracy.

8.2 Arbitrarily eccentric, coplanar orbits

8.2.1 Expressions for ψ

By using the Cartesian elements $(x_{12}, y_{12}, z_{12}, x_{13}, y_{13}, z_{13})$ computed from the equations in Appendix A, I now obtain expressions for ψ through equation (56). The 1S2P case simplifies to:

$$\psi^{\rm (e)}_{\rm 1S2P} = \left[\mathfrak{n}_{12}\,(t-\tau_{12}) - \mathfrak{n}_{13}\,(t-\tau_{13})\right]. \tag{115}$$

The 2S1P case does not feature such fortunate cancellations, as the resulting expression for ψ becomes a function of both time and true anomaly through $r_{12}(\Pi)$ and $r_{123}(\Pi)$:

$$\cos\psi^{\rm (e)}_{\rm 2S1P} = \frac{\frac{M_1}{M_1+M_2}r^{\rm (e)}_{\rm 12,2S1P} + r^{\rm (e)}_{\rm 123,2S1P}\cos\left[\mathfrak{n}_{12}\,(t-\tau_{12}) - \mathfrak{n}_{123}\,(t-\tau_{123})\right]}{r^{\rm (e)}_{\rm 13,2S1P}}, \tag{116}$$

where

$$\left(r^{\rm (e)}_{\rm 13,2S1P}\right)^2 = \left(\frac{M_1}{M_1+M_2}\right)^2\left(r^{\rm (e)}_{\rm 12,2S1P}\right)^2 + \left(r^{\rm (e)}_{\rm 123,2S1P}\right)^2 + \frac{M_1 r^{\rm (e)}_{\rm 12,2S1P} r^{\rm (e)}_{\rm 123,2S1P}\cos\left[\mathfrak{n}_{12}\,(t-\tau_{12}) - \mathfrak{n}_{123}\,(t-\tau_{123})\right]}{M_1+M_2}. \tag{117}$$

The two cases which include moons are more compact but feature the same dependencies on time and true anomaly through, for the moon occulter, $r_{13}(\Pi)$ and $r_{23}(\Pi)$:

$$\cos\psi^{\rm (e)}_{\rm 1M-MO} = \frac{r^{\rm (e)}_{\rm 13,1M-MO} - r^{\rm (e)}_{\rm 23,1M-MO}\cos\left[\mathfrak{n}_{13}\,(t-\tau_{13}) - \mathfrak{n}_{23}\,(t-\tau_{23})\right]}{r^{\rm (e)}_{\rm 12,1M-MO}}, \tag{118}$$

where

$$\left(r^{\rm (e)}_{\rm 12,1M-MO}\right)^2 = \left(r^{\rm (e)}_{\rm 13,1M-MO}\right)^2 + \left(r^{\rm (e)}_{\rm 23,1M-MO}\right)^2 - 2r^{\rm (e)}_{\rm 13,1M-MO} r^{\rm (e)}_{\rm 23,1M-MO}\cos\left[\mathfrak{n}_{13}\,(t-\tau_{13}) - \mathfrak{n}_{23}\,(t-\tau_{23})\right], \tag{119}$$

and for the planet occulter, $r_{12}(\Pi)$ and $r_{23}(\Pi)$:

$$\cos\psi^{\rm (e)}_{\rm 1M-PO} =$$

$$\frac{r^{(\mathrm{e})}_{12,1\mathrm{M-PO}} + r^{(\mathrm{e})}_{23,1\mathrm{M-PO}} \cos\left[\mathfrak{n}_{12}\left(t-\tau_{12}\right) - \mathfrak{n}_{23}\left(t-\tau_{23}\right)\right]}{r^{(\mathrm{e})}_{13,1\mathrm{M-PO}}}, \tag{120}$$

where

$$\left(r^{(\mathrm{e})}_{13,1\mathrm{M-PO}}\right)^2 = \left(r^{(\mathrm{e})}_{12,1\mathrm{M-PO}}\right)^2 + \left(r^{(\mathrm{e})}_{23,1\mathrm{M-PO}}\right)^2 + 2r^{(\mathrm{e})}_{12,1\mathrm{M-PO}} r^{(\mathrm{e})}_{23,1\mathrm{M-PO}} \cos\left[\mathfrak{n}_{12}\left(t-\tau_{12}\right) - \mathfrak{n}_{23}\left(t-\tau_{23}\right)\right]. \tag{121}$$

8.2.2 Solving for time

Regardless if the angle ψ is given by equations (115), (116), (118) or (120), in the arbitrarily eccentric case, comparison with equations (57) and (60) will yield additional dependencies on true anomaly. In these instances, Kepler's (implicit) equation must be solved at every instance along the orbits until the angles are found to overlap.

8.3 Circular, arbitrarily inclined orbits

In order to aid readability, many of the expressions in this section can be simplified by utilising the following auxiliary variables

$$\begin{aligned}
\mathcal{S}_{12} &\equiv \sin\left[\mathfrak{n}_{12}\left(t-\tau_{12}\right) + w_{12}\right], && (122)\\
\mathcal{S}_{13} &\equiv \sin\left[\mathfrak{n}_{13}\left(t-\tau_{13}\right) + w_{13}\right], && (123)\\
\mathcal{S}_{23} &\equiv \sin\left[\mathfrak{n}_{23}\left(t-\tau_{23}\right) + w_{23}\right], && (124)\\
\mathcal{S}_{123} &\equiv \sin\left[\mathfrak{n}_{123}\left(t-\tau_{123}\right) + w_{123}\right], && (125)\\
\mathcal{C}_{12} &\equiv \cos\left[\mathfrak{n}_{12}\left(t-\tau_{12}\right) + w_{12}\right], && (126)\\
\mathcal{C}_{13} &\equiv \cos\left[\mathfrak{n}_{13}\left(t-\tau_{13}\right) + w_{13}\right], && (127)\\
\mathcal{C}_{23} &\equiv \cos\left[\mathfrak{n}_{23}\left(t-\tau_{23}\right) + w_{23}\right], && (128)\\
\mathcal{C}_{123} &\equiv \cos\left[\mathfrak{n}_{123}\left(t-\tau_{123}\right) + w_{123}\right], && (129)\\
\mathcal{P}_{12} &\equiv \mathcal{C}_{12}\sin\Omega_{12} + \mathcal{S}_{12}\cos\Omega_{12}\cos i_{12}, && (130)\\
\mathcal{P}_{123} &\equiv \mathcal{C}_{123}\sin\Omega_{123} + \mathcal{S}_{123}\cos\Omega_{123}\cos i_{123}, && (131)\\
\mathcal{U}_{12} &\equiv \mathcal{C}_{12}\cos\Omega_{12} - \mathcal{S}_{12}\sin\Omega_{12}\cos i_{12}, && (132)\\
\mathcal{U}_{123} &\equiv \mathcal{C}_{123}\cos\Omega_{123} - \mathcal{S}_{123}\sin\Omega_{123}\cos i_{123}. && (133)
\end{aligned}$$

Although I could simplify the above expressions slightly by considering the plane of one of the orbits to be the reference plane, the complete expressions can be more easily used in conjunction with given sets of orbital parameter data.

8.3.1 Expressions for ψ

The following equations are slightly cumbersome, but are useful for direct computation and do illustrate how even circularity does not allow for simple functions of ψ. Time appears in multiple locations in each of the equations, but all explicitly, as opposed to implicitly through Π and r as in the eccentric case. For one star and two planets, I obtain

$$\begin{aligned}
\cos\psi^{(\mathrm{i})}_{1\mathrm{S2P}} = {} & \left[\mathcal{C}_{12}\mathcal{C}_{13} + \mathcal{S}_{12}\mathcal{S}_{13}\cos i_{12}\cos i_{13}\right]\cos\left[\Omega_{12}-\Omega_{13}\right]\\
& + \left[\mathcal{C}_{12}\mathcal{S}_{13}\cos i_{13} - \mathcal{S}_{12}\mathcal{C}_{13}\cos i_{12}\right]\sin\left[\Omega_{12}-\Omega_{13}\right]\\
& + \mathcal{S}_{12}\mathcal{S}_{13}\sin i_{12}\sin i_{13}. \qquad (134)
\end{aligned}$$

For two stars and one planet, the mass of both stars is introduced as usual and I obtain

$$\begin{aligned}
\cos\psi^{(\mathrm{i})}_{2\mathrm{S1P}} = {} & \left[\frac{1}{\left(M_1+M_2\right) r^{(\mathrm{i})}_{13,2\mathrm{S1P}}}\right]\\
& \times\Bigg[M_1 a_{12}\left(\mathcal{P}_{12}^2 + \mathcal{U}_{12}^2\right)\\
& + \left(M_1+M_2\right) a_{123}\left(\mathcal{P}_{12}\mathcal{P}_{123} + \mathcal{U}_{12}\mathcal{U}_{123}\right)\\
& + \mathcal{S}_{12}\sin i_{12}\left[M_1 a_{12}\mathcal{S}_{12}\sin i_{12} + \left(M_1+M_2\right) a_{123}\mathcal{S}_{123}\sin i_{123}\right]\Bigg], \qquad (135)
\end{aligned}$$

where

$$\begin{aligned}
\left(r^{(\mathrm{i})}_{13,2\mathrm{S1P}}\right)^2 = {} & a_{123}^2 + \frac{M_1^2 a_{12}^2}{\left(M_1+M_2\right)^2} + \frac{2M_1 a_{12} a_{123}}{M_1+M_2}\\
& \times\Bigg[\left(\mathcal{C}_{12}\mathcal{C}_{123} + \mathcal{S}_{12}\mathcal{S}_{123}\cos i_{12}\cos i_{123}\right)\cos\left[\Omega_{12}-\Omega_{123}\right]\\
& + \left(\mathcal{C}_{12}\mathcal{S}_{123}\cos i_{123} - \mathcal{S}_{12}\mathcal{C}_{123}\cos i_{12}\right)\sin\left[\Omega_{12}-\Omega_{123}\right]\\
& + \mathcal{S}_{12}\mathcal{S}_{123}\sin i_{12}\sin i_{123}\Bigg]. \qquad (136)
\end{aligned}$$

The importance of inclination for the cases which include a moon are highlighted by Earth-Moon-Sun eclipses, where inclination plays a large role in determining whether a system is in transit. For the moon occulter,

$$\begin{aligned}
\cos\psi^{(\mathrm{i})}_{1\mathrm{M-MO}} = {} & \frac{1}{r^{(\mathrm{i})}_{12,1\mathrm{M-MO}}}\Bigg[-a_{23}\mathcal{C}_{13}\mathcal{C}_{23}\cos\left(\Omega_{13}-\Omega_{23}\right) + a_{13}\\
& - a_{23}\mathcal{S}_{13}\mathcal{S}_{23}\left(\cos i_{13}\cos i_{23}\cos\left[\Omega_{13}-\Omega_{23}\right] + \sin i_{13}\sin i_{23}\right)\\
& + a_{23}\sin\left[\Omega_{13}-\Omega_{23}\right]\left(\mathcal{C}_{23}\mathcal{S}_{13}\cos i_{13} - \mathcal{C}_{13}\mathcal{S}_{23}\cos i_{23}\right)\Bigg], \qquad (137)
\end{aligned}$$

with

$$\begin{aligned}
\left(r^{(\mathrm{i})}_{12,1\mathrm{M-MO}}\right)^2 = {} & a_{13}^2 + a_{23}^2\\
& + 2a_{13}a_{23}\Bigg[-\mathcal{C}_{13}\mathcal{C}_{23}\cos\left(\Omega_{13}-\Omega_{23}\right)\\
& - \mathcal{S}_{13}\mathcal{S}_{23}\left(\cos i_{13}\cos i_{23}\cos\left[\Omega_{13}-\Omega_{23}\right] + \sin i_{13}\sin i_{23}\right)\\
& + \sin\left[\Omega_{13}-\Omega_{23}\right]\left(\mathcal{C}_{23}\mathcal{S}_{13}\cos i_{13} - \mathcal{C}_{13}\mathcal{S}_{23}\cos i_{23}\right)\Bigg], \qquad (138)
\end{aligned}$$

whereas for the planet occulter,

$$\begin{aligned}
\cos\psi^{(\mathrm{i})}_{1\mathrm{M-PO}} = {} & \frac{1}{r^{(\mathrm{i})}_{13,1\mathrm{M-PO}}}\Bigg[a_{23}\mathcal{C}_{12}\mathcal{C}_{23}\cos\left(\Omega_{12}-\Omega_{23}\right) + a_{12}\\
& + a_{23}\mathcal{S}_{12}\mathcal{S}_{23}\left(\cos i_{12}\cos i_{23}\cos\left[\Omega_{12}-\Omega_{23}\right] + \sin i_{12}\sin i_{23}\right)\\
& + a_{23}\sin\left[\Omega_{12}-\Omega_{23}\right]\left(-\mathcal{C}_{23}\mathcal{S}_{12}\cos i_{12} + \mathcal{C}_{12}\mathcal{S}_{23}\cos i_{23}\right)\Bigg], \qquad (139)
\end{aligned}$$

with

$$\left(r^{(\mathrm{i})}_{13,1\mathrm{M-PO}}\right)^2 = a_{12}^2 + a_{23}^2$$
$$+2a_{12}a_{23}\Bigg[\mathcal{C}_{12}\mathcal{C}_{23}\cos\left(\Omega_{12}-\Omega_{23}\right)$$
$$+\mathcal{S}_{12}\mathcal{S}_{23}\left(\cos i_{12}\cos i_{23}\cos\left[\Omega_{12}-\Omega_{23}\right]+\sin i_{12}\sin i_{23}\right)$$
$$+\sin\left[\Omega_{12}-\Omega_{23}\right]\left(-\mathcal{C}_{23}\mathcal{S}_{12}\cos i_{12}+\mathcal{C}_{12}\mathcal{S}_{23}\cos i_{23}\right)\Bigg]. \quad (140)$$

8.3.2 Solving for time

For circular orbits, Kepler's equation need not be solved in order to determine transit durations and frequencies. All which is required is an implicit solution for time in the relations between ψ and $\psi_{\blacklozenge}$ (and $\psi_{\diamond}$). Then the answer in terms of transit durations and frequencies is immediate.

8.4 Circular, coplanar orbits

In the simplest, but often representative, case of circular coplanar orbits, the equations are simpler, and for the 1S2P case, I obtain explicit closed-form solutions.

8.4.1 Expressions for ψ

I find

$$\psi^{(\mathrm{cc})}_{1\mathrm{S2P}} = \psi^{(\mathrm{e})}_{1\mathrm{S2P}} \quad (141)$$

and

$$\cos\psi^{(\mathrm{cc})}_{2\mathrm{S1P}} = \left(\frac{1}{r^{(\mathrm{cc})}_{13,1\mathrm{S2P}}}\right)\Bigg[M_1 a_{12} + (M_1+M_2) \times a_{123}\cos\left[\mathfrak{n}_{12}\left(t-\tau_{12}\right)-\mathfrak{n}_{123}\left(t-\tau_{123}\right)\right]\Bigg], \quad (142)$$

with

$$\left(r^{(\mathrm{cc})}_{13,1\mathrm{S2P}}\right)^2 = M_1^2 a_{12}^2 + (M_1+M_2)^2 a_{123}^2$$
$$+2a_{12}a_{123}M_1\left(M_1+M_2\right)\cos\left[\mathfrak{n}_{12}\left(t-\tau_{12}\right)-\mathfrak{n}_{123}\left(t-\tau_{123}\right)\right]. \quad (143)$$

For the moon occulter,

$$\cos\psi^{(\mathrm{cc})}_{1\mathrm{M-MO}} = \frac{a_{13}-a_{23}\cos\left[\mathfrak{n}_{13}\left(t-\tau_{13}\right)-\mathfrak{n}_{23}\left(t-\tau_{23}\right)\right]}{\sqrt{a_{13}^2+a_{23}^2-2a_{13}a_{23}\cos\left[\mathfrak{n}_{13}\left(t-\tau_{13}\right)-\mathfrak{n}_{23}\left(t-\tau_{23}\right)\right]}}, \quad (144)$$

whereas for the planet occulter,

$$\cos\psi^{(\mathrm{cc})}_{1\mathrm{M-PO}} = \frac{a_{12}+a_{23}\cos\left[\mathfrak{n}_{12}\left(t-\tau_{12}\right)-\mathfrak{n}_{23}\left(t-\tau_{23}\right)\right]}{\sqrt{a_{12}^2+a_{23}^2+2a_{12}a_{23}\cos\left[\mathfrak{n}_{12}\left(t-\tau_{12}\right)-\mathfrak{n}_{23}\left(t-\tau_{23}\right)\right]}}. \quad (145)$$

8.4.2 Solving for time

Solving for time does not require the solution of Kepler's equation, and time appears in the above expressions for ψ in just a single cosine argument. However, the time dependencies of $\psi_{\blacklozenge}$ and $\psi_{\diamond}$ are too complex for explicit solutions, except in the 1S2P case.

In the 1S2P case, $r_{12}(t) = a_{12}$ and $r_{13}(t) = a_{13}$. Consequently umbral and antumbral transits begin according to equation (57) such that the pth transit starts at the following time

$$\mathfrak{s}^{(p)}_{1\mathrm{S2P}} = \frac{\mathfrak{n}_{12}\tau_{12}-\mathfrak{n}_{13}\tau_{13}+2\pi\left(p-1\right)-\left|\psi_{\blacklozenge}\right|}{\mathfrak{n}_{12}-\mathfrak{n}_{13}} \quad (146)$$

and ends at

$$\mathfrak{e}^{(p)}_{1\mathrm{S2P}} = \frac{\mathfrak{n}_{12}\tau_{12}-\mathfrak{n}_{13}\tau_{13}+2\pi\left(p-1\right)+\left|\psi_{\blacklozenge}\right|}{\mathfrak{n}_{12}-\mathfrak{n}_{13}} \quad (147)$$

The duration of each transit is then

$$\mathfrak{d}^{(p)}_{1\mathrm{S2P}} = \mathfrak{e}^{(p)}_{1\mathrm{S2P}} - \mathfrak{s}^{(p)}_{1\mathrm{S2P}} = \frac{2\left|\psi_{\blacklozenge}\right|}{\mathfrak{n}_{12}-\mathfrak{n}_{13}}, \quad (148)$$

the duration of ingress and egress is

$$\mathfrak{D}^{(p)}_{1\mathrm{S2P}} = \frac{\left|\psi_{\blacklozenge}\right|-\left|\psi_{\diamond}\right|}{\mathfrak{n}_{12}-\mathfrak{n}_{13}} \quad (149)$$

and the frequency of transits is given by

$$\mathfrak{f}_{1\mathrm{S2P}} = \mathfrak{s}^{(p+1)}_{1\mathrm{S2P}} - \mathfrak{s}^{(p)}_{1\mathrm{S2P}} = \frac{2\pi}{\mathfrak{n}_{12}-\mathfrak{n}_{13}}. \quad (150)$$

9 PARTIAL ECLIPSES

The entire paper so far has focused on total and annular eclipses. However, another type of eclipse – a partial eclipse – always accompanies a total or annular eclipse. A partial eclipse is formed through the internal tangent lines (as opposed to the external tangent lines) between the primary and occulter (see Fig. 19, which is reproduced from figure 2 of Paper I).

The geometry of partial eclipses is akin to that of annular eclipses because the target intersects the upper nappe of the radiation cone. The similarities between these two types of eclipses of syzygy were highlighted in Appendix B of Paper I. There it was revealed that several of the quantities for the penumbral cone could be reproduced by replacing R_2 with $-R_2$ in the corresponding antumbral cone.

I use this symmetry here to great effect. Rather than rework all of the results so far with this different cone, all I need to do is define

$$\Delta \equiv \frac{R_1+R_2}{r_{12}}, \quad (151)$$

and then replace δ with Δ in all of the relevant equations.

9.1 Condition to be in transit

Replacing δ with Δ in the equation of the intersection (equations 27-36) is valid, as can be shown by establishing the equation of the penumbral radiation cone and expressing it as a quadric. Hence, the conditions to be in transit and fully engulfed in the shadow (equations 57 and 60) are the same except for δ being replaced by Δ.

Whether or not the system is in transit with respect to

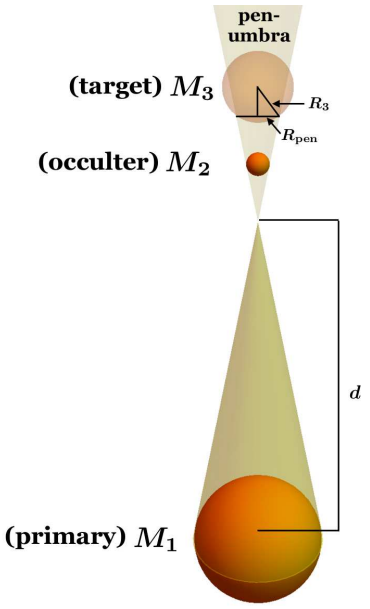

Figure 19. The radiation cone producing the penumbral shadow, with the target at syzygy. Comparison with Fig. 3 illustrates the difference in geometry with the umbral and antumbral cases. This figure is a reproduction of figure 2 of Paper I.

the penumbral shadow is of particular interest because observers on the target will first start to see the primary being obscured during a partial (not total nor annular) eclipse.

9.2 Shape of the shadow

For the penumbral case, the ranks of the matrices in equations (38) and (39) are still three and one, respectively. Consequently, the penumbral shadow is always a parabolic cylinder, like both the umbral and antumbral shadows.

9.3 Size of the shadow

In the expressions for the size of the antumbral shadow, δ appears through $\mathcal{F}$ (equation 72), $\mathcal{G}^\vee$ (equation 74) and $\omega^\vee$ (equations 75-76). Replacing δ with Δ accounts for all of the differences between the penumbral and antumbral shadows.

9.4 Time evolution

The starting and ending times of transits for the penumbral shadow will be different from the antumbral or umbral cases because the penumbral shadow is much larger.

The difference in these times can be computed explicitly for the circular, coplanar case of two planets and one star. In order to compute $\mathfrak{s}$, $\mathfrak{e}$ and $\mathfrak{d}$ for the penumbral case, just replace δ with Δ. Then, for example, an observer on a planetary target who just sees the primary start to be obscured by another planet must wait for a time equal to

$$\frac{|\cos\psi_\blacklozenge\left(\delta\to\Delta\right)|-|\cos\psi_\blacklozenge\left(\delta\right)|}{\mathfrak{n}_{12}-\mathfrak{n}_{13}}, \tag{152}$$

before being able to witness the start of the total or annular eclipse.

10 EXTERNAL VIEW OF A SYZYGY

Having considered the three-body case in some detail, I now finish the main text of the paper by exploring an extension to the four-body case under the same formalism. In order to keep this analysis manageable, throughout the section at least the primary, occulter and target are assumed to be in syzygy. My analysis here could be particularly relevant to mutual occultation events between exoplanets as viewed from Earth, as recently described by Luger et al. (2017), or, for example, to observing both Phobos and Deimos from the surface of Mars when both moons are in syzygy with the Sun.

A key initial question is, does the occulter or the target block the primary's light from reaching the external body? The answer depends on the relative sizes and distances of the bodies. I denote the external body as the #4 body, and r_{14} as the centre-to-centre distance between that body and the primary.

10.1 Co-linear syzygy

If the observer on the external body is co-linear with the syzygy, then Fig. 20 reveals (given a fixed r_{12}) the critical distance $r_{23}^{\uplus}$ beyond which ($r_{23} > r_{23}^{\uplus}$) the target, rather than the occulter, is responsible for blocking the primary's starlight. The geometry of similar triangles illustrates

$$\frac{R_2}{r_{14}-R_4-r_{12}}=\frac{R_3}{r_{14}-R_4-r_{12}-r_{23}^{\uplus}} \tag{153}$$

which reduces to

$$r_{23}^{\uplus}=\frac{R_2-R_3}{R_2}\left(r_{14}-R_4-r_{12}\right), \tag{154}$$

an expression which is independent of R_1.

Let the angular diameter that the observer (or observatory) sees be η such that the angular diameter of the shadow on the primary is $\eta_{\rm sha}$. Then

$$\eta_{\rm sha}=2\min\left[\sin^{-1}\left(\frac{R_3}{r_{14}-r_{13}-R_4}\right),\ \sin^{-1}\left(\frac{R_1}{r_{14}-R_4}\right)\right],$$
$$r_{23}\geqslant r_{23}^{\uplus}$$
$$\eta_{\rm sha}=2\min\left[\sin^{-1}\left(\frac{R_2}{r_{14}-r_{12}-R_4}\right),\ \sin^{-1}\left(\frac{R_1}{r_{14}-R_4}\right)\right],$$
$$r_{23}<r_{23}^{\uplus}. \tag{155}$$

10.2 Offset syzygy

Now consider the case when the external body is not co-linear with the syzygy – but still co-planar with it – and offset from the syzygy by a perpendicular distance $k>0$. Note that in this case, the distance r_{14} is not parallel to the syzygy.

10.2.1 No eclipse

I first consider the limiting value $k_\forall$ for which an observer would not see any eclipse at all (neither from the occulter, target, nor both). Fig. 21 illustrates the geometry for this limiting value. The images on the left side of the figure are zoomed-in, angularly exaggerated portions of the overall geometry. I find

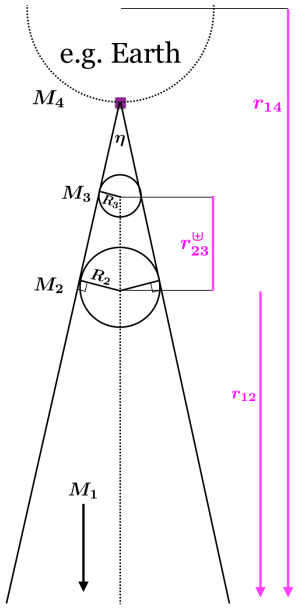

Figure 20. A snapshot of an observer (square) standing on an object (M_4; such as the Earth) which is external to but co-linear with a syzygy (e.g. two exoplanets as M_2 and M_3 and their host star as M_1, or two solar system planets M_2 and M_3 with the Sun as M_1). Shown in this diagram is the limiting case in which both the occulter and target produce the same-sized shadow on the disk of the primary in sky. For $r_{23} > r_{23}^{\uplus}$, the target would produce the shadow, whereas for $r_{23} < r_{23}^{\uplus}$, the occulter would produce the shadow. Equations (153-155) are derived from this diagram.

$$\cos\chi = \frac{R_1}{d+u} = \frac{R_3 - R_2}{r_{23}^*} = \frac{R_4 - \sqrt{R_4^2 - k_\forall^2}}{\sqrt{\left(R_4 - \sqrt{R_4^2 - k_\forall^2}\right)^2 + k_\forall^2}} \tag{156}$$

which gives

$$k_\forall = \frac{2R_4\left(R_1 + R_2\right)}{r_{12}^2}\sqrt{r_{12}^2 - \left(R_1 + R_2\right)^2} \tag{157}$$

$$= \frac{2R_4\left(R_2 - R_3^*\right)}{r_{23}^2}\sqrt{r_{23}^2 - \left(R_2 - R_3^*\right)^2}. \tag{158}$$

Here, d and u are the penumbral equivalents to h and n from Paper I, and r_{23}^* is the critical value of r_{23} beyond which the target is engulfed in the penumbral shadow (equation B8 of Paper I). I conclude here that when $k \geqslant k_\forall$ at $R_3 = R_3^*$, or when $R_3 \leqslant R_3^*$ at $k = k_\forall$, then the observer cannot see any type of eclipse.

10.2.2 Some eclipse

In contrast, when $k < k_\forall$ at $R_3 = R_3^*$, or when $R_3 > R_3^*$ at $k = k_\forall$, then the observer will see some type of eclipse. Here, I compute two limiting values, when the target and occulter are entirely within the field of view on the side of the offset (Fig. 22) and on the opposite side (Fig. 23). I denote these limiting values as $k_\sqcup$ and $k_\parallel$, respectively, and note that the later can occur only when $k < R_1$ and either $k < R_2$ or $k < R_3$.

The geometry from Fig. 22 reveals

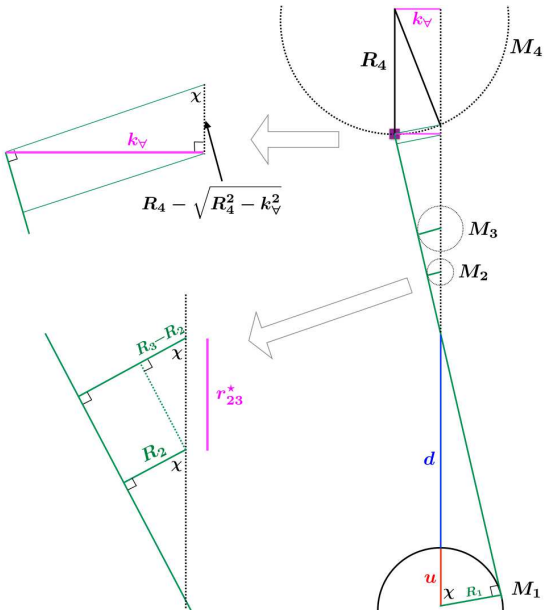

Figure 21. A snapshot of an observer (square) standing on an object (M_4) which is external to, offset from, and coplanar with a syzygy. This diagram illustrates the limiting case where both the occulter and target remain just undetectable (at $k = k_\forall$ and $r_{23} = r_{23}^*$). Equations (156-158) are derived from this diagram.

$$\cos\zeta = \frac{R_1}{h+n} = \frac{R_2 - R_3}{r_{23}^\dagger} = \frac{R_4 - \sqrt{R_4^2 - k_\sqcup^2}}{\sqrt{\left(R_4 - \sqrt{R_4^2 - k_\sqcup^2}\right)^2 + k_\sqcup^2}} \tag{159}$$

which yields

$$k_\sqcup = \frac{2R_4\left(R_1 - R_2\right)}{r_{12}^2}\sqrt{r_{12}^2 - \left(R_1 - R_2\right)^2} \tag{160}$$

$$= \frac{2R_4\left(R_2 - R_3^\dagger\right)}{r_{23}^2}\sqrt{r_{23}^2 - \left(R_2 - R_3^\dagger\right)^2} \tag{161}$$

and the geometry from Fig. 23 reveals

$$\cos\iota = \frac{R_1}{h+n} = \frac{R_2 - R_3}{r_{23}^\dagger} = \frac{k_\parallel}{\sqrt{\left(h + n + R_4 - \sqrt{r_{14}^2 - k_\parallel^2}\right)^2 + k_\parallel^2}} \tag{162}$$

giving

$$k_\parallel^2 = (h+n+R_4)^2\left[\left(\frac{R_1}{h+n}\right)^2 - 2\left(\frac{R_1}{h+n}\right)^4\right]$$

$$+\left(\frac{R_1 r_{14}}{h+n}\right)^2 - \frac{2R_1^2\left(h+n+R_4\right)}{(h+n)^4}\left\{\left[R_1^2 - (h+n)^2\right]\right.$$

$$\left.\times\left[(h+n)^2\left(R_1^2 - r_{14}^2\right) + R_4 R_1^2\left[2\left(h+n\right) + R_4\right]\right]\right\}^{\frac{1}{2}}. \tag{163}$$

Consequently, the side of the primary which is in the same direction of the offset will be obscured if $k_\sqcup < k < k_\forall$. In order for the side of the primary opposite the offset to be obscured, then $k < k_\parallel$.

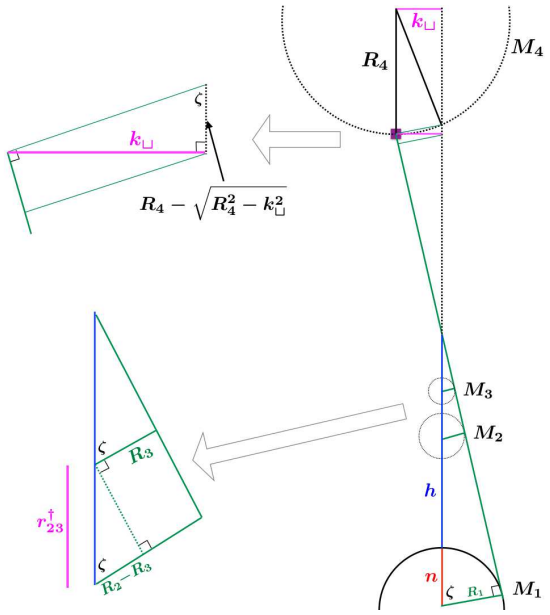

Figure 22. A snapshot of an observer (square) standing on an object (M_4) which is external to, offset from, and coplanar with an syzygy. This diagram illustrates the limiting case where both the occulter and target appear just fully inside of the disc on the side of the offset (at $k = k_\sqcup$ and $r_{23} = r_{23}^\dagger$). Equations (159-161) are derived from this diagram.

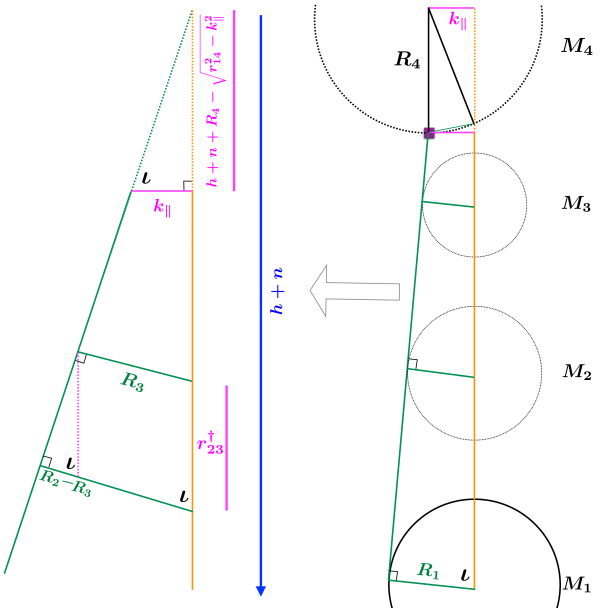

Figure 23. A snapshot of an observer (square) standing on an object (M_4) which is external to, offset from, and coplanar with an syzygy. This diagram illustrates the limiting case where both the occulter and target appear just fully inside of the disc on the side opposite the offset (at $k = k_\parallel$ and $r_{23} = r_{23}^\dagger$). Equations (162-163) are derived from this diagram.

10.2.3 Angular diameters

For an offset syzygy, the angular diameters of the primary, occulter and target could all be computed in similar ways, by analogy with the offset observer from Fig. A3 of Paper I. The left panel of Fig. 24 illustrates the relevant geometry for an arbitrary value of k, and yields

$$\eta_{14} = 2\sin^{-1}\left[\frac{R_1}{\sqrt{k^2 + \left(\sqrt{r_{14}^2 - k^2} - R_4\right)^2}}\right]. \tag{164}$$

Similar formulae hold for η_{24} and η_{34}.

10.2.4 Double annular eclipses

Much trickier is the prospect of computing $\eta_{\rm sha}$ by combining the angular diameters of the three objects in syzygy when they overlap in the sky. I do not delve into the details of various configurations, except for the interesting case when both the occulter and target are simultaneously visible as distinct discs at some point during eclipse. This situation is, in effect, a double annular eclipse.

To determine limiting values of k and r_{23} (denoted as $k_\bullet$ and $r_{23}^\bullet$) which can produce such a configuration, consider the right panel of Fig. 24. First I helpfully define the length of the line extending from the observer to either tangent point of any of the bodies in syzygy as

$$l_{14} \equiv \sqrt{\left(\sqrt{r_{14}^2 - k_\bullet^2} - R_4\right)^2 + k_\bullet^2 - R_1^2}, \tag{165}$$

$$l_{24} \equiv \sqrt{\left[\sqrt{r_{14}^2 - k_\bullet^2} - R_4 - r_{12}\right]^2 + k_\bullet^2 - R_2^2}, \tag{166}$$

$$l_{34} \equiv \sqrt{\left[\sqrt{r_{14}^2 - k_\bullet^2} - R_4 - r_{13}\right]^2 + k_\bullet^2 - R_3^2}. \tag{167}$$

Next, consider the two triangles formed by the orange, black, blue and lower horizontal magenta lines such that the bottom triangle partially intersects M_3. The lengths of the orange line is l_{34}, the magenta line is $k_\bullet$ and the blue line is R_3. The lower part of the orange line (in the bottom triangle) is then given by

$$l_{34}^{(\rm lower)} = \left(\frac{R_3}{k_\bullet^2 - R_3^2}\right)\left[k_\bullet\sqrt{l_{34}^2 + R_3^2 - k_\bullet^2} - R_3 l_{34}\right]. \tag{168}$$

Now I obtain a relation based on similar triangles: one of which being the bottom of the aforementioned triangles, and the other being the downward extension of that triangle to the primary. That comparison yields

$$\frac{l_{34}^{(\rm lower)}}{R_3} = \frac{l_{14} - l_{34} + l_{34}^{(\rm lower)}}{R_1}, \tag{169}$$

which is an implicit equation for $k_\bullet$, and for which $k_\bullet$ can be numerically determined.

In order to relate $k_\bullet$ to $r_{23}^\bullet$, consider the brown line, which has length $l_{24} - l_{34}$, and the two triangles formed by its intersection with the vertical magenta line of length $r_{23}^\bullet$. The upper part of this magenta line has length $[R_3 r_{23}^\bullet / (R_2 + R_3)]$ and the upper part of the brown line has length $[R_3 (l_{24} - l_{34}) / (R_2 + R_3)]$. The Pythagorean theorem then gives the following relation:

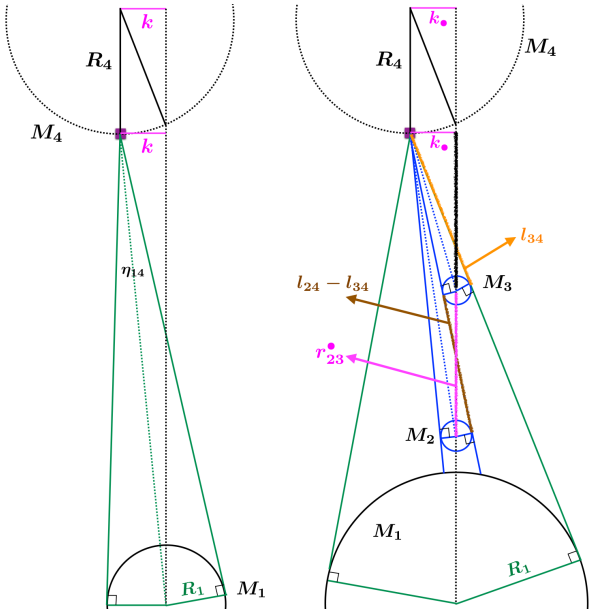

Figure 24. A snapshot of an observer (square) standing on an object (M_4) which is external to, offset from, but coplanar with an syzygy. The left-hand panel illustrates how the angular diameter for one of the objects (the primary here) can be derived. The right-hand panel illustrates the limiting case where both the occulter and target appear entirely, simultaneously and non-overlapping on the disc of the primary in the sky (for $k \geqslant k_\bullet$ and $r_{23} \geqslant r^\bullet_{23}$). Equations (164-170) are derived from this diagram.

$$\left(r^\bullet_{23}\right)^2 = \left(R_2 + R_3\right)^2 + \left(l_{24} - l_{34}\right)^2 . \qquad (170)$$

10.2.5 Observing solar system syzygys

Sometimes, the Sun, Mercury, Venus and Earth will all be in syzygy. In this case, equation (154) reveals that $r^{\Psi}_{23} < 0$, which indicates that Venus – and not Mercury – will block the Sun's light from a viewer on Earth. If the Earth is coplanar to but not co-linear with the syzygy formed by the Sun, Mercury and Venus, then I consider the quantities $k_\forall$, $k_\sqcup$ and $k_\parallel$ from equations (158), (160) and (163). I find $k_\parallel > R_1$, and so the situation in Fig. 23 cannot occur. Also, $k_\forall = 153.56$ km and $k_\sqcup = 152.49$ km, meaning that an observer on Earth would have to be within 153.56 km of the syzygy in order to see it, and can see just one side of the Sun being blocked only at an offset which is in-between 152.49 km and 153.56 km.

10.2.6 Observing extrasolar system syzygys

In extrasolar planetary systems like Kepler-47 (featured in Paper I), with two stars (Kepler-47A and Kepler-47B) on a tight orbit and two planets (Kepler-47ABb and Kepler-47ABc), syzygys might be common amongst three, or even all four bodies in the system. In a four-body syzygy, an observatory on the outer planet (Kepler-47ABc) will see light blocked from the primary due to the companion star, and not due to the inner planet, because $r^{\Psi}_{23} > r_{23}$. If the outer planet is offset from but still coplanar with the syzygy of the other three bodies[5], then $k_\forall = 4270$ km and $k_\sqcup = 2000$ km. If $k < k_\forall$, then the observatory will detect the syzygy. If $k_\sqcup < k < k_\forall$, then the observatory will see obscuration of the side of the primary that is on the same side of the offset. This wide range is due to the large (stellar) size of the occulter. Because $k_\parallel > R_1$, the situation in Fig. 23 cannot hold. What about a person standing on Earth observing Kepler-47A, Kepler-47B and Kepler-47ABb when they are in syzygy? If the Earth would be coplanar with this syzygy, then $k_\forall = 929$ km and $k_\sqcup = 434$ km.

11 SUMMARY

I have derived user-friendly algebraic relations and criteria for eclipses, transits and occultations, having been inspired by the foundational geometry of Veras & Breedt (2017). These relations may be useful for a variety of purposes for transit identification, in the planning and analysis of observations, and for an understanding of the shadowing conditions on the surfaces and atmospheres of planets and moons; Figs. 1 and 2 contain flowcharts for quick use. Because nearly all formulae are independent of perspective, they may be applied to Earth-based observatories, Solar system-based observatories (on land and in space), and observatories within extrasolar systems.

My focus was on three-body systems which include one star, one planet, and one other body which could be a star, planet or moon. The only major assumptions I made about these bodies were that they are all spheres, that light rays do not bend, and for orbital motion cases, that the orbits are fixed. I considered both snapshots of these systems (Sections 3-7) and their motion (Section 8, and Appendices A and B) in the context of umbral, antumbral and penumbral (Section 9) shadows. I also illustrated how some of these results may be extended to four bodies, with an observer situated on the fourth external body, such as the Earth (Section 10).

For snapshots in time, specific results include

(i) A criterion to determine if a given system architecture is in or out of transit (equation 57),

(ii) If in transit, whether the target will be fully engulfed in the shadow (equation 60),

(iii) Whether a specific location on the target is in transit (equation 66),

(iv) Whether or not the shadow is umbral or antumbral (equation 69); a penumbral shadow will always accompany both,

(v) The size of the umbral shadow (equation 110) or antumbral shadow (equation 111),

(vi) The minimum shadow size (equations 95-96) and maximum shadow size (equations 97-98), and

(vii) A transformation (from equation 14 to equation 151) which enables one to obtain snapshot results for penumbral cones without having to perform derivations similar to those carried out for the umbral and antumbral cones.

[5] As of 29 October 2018, the inclination constraints on both planets from the Exoplanet Data Explorer (at exoplanets.org) are still consistent with the possibility of coplanarity.

Of more mathematical interest is

(viii) That the shadow is always a parabolic cylinder (Section 4),

(ix) The equation of the intersection of the radiation cone and spherical target in Cartesian coordinates (equations 27-37) and in radial coordinates (equation 40), and

(x) The transformed version of this equation in standard form (equation 41).

For time evolution, specific results include

(i) Start times, end times, durations and frequencies of transits (including ingresses and egresses) for two planets on circular coplanar orbits around a star (equations 146-150),

(ii) The angles ψ which allow for a single implicit computation of start times, end times, durations and frequencies of transits for circular arbitrarily inclined orbits (equations 134-139), and

(iii) The angles ψ which allow for implicit computation of transit properties for arbitrarily eccentric, coplanar orbits (equations 115-120).

For the special extended case of an observer of an exosyzygy, specific results include

(i) The critical distance beyond which the target, rather than the occulter, blocks the primary's starlight (equation 154),

(ii) The maximum allowable transverse distance of the observer (perpendicular to the syzygy; equations 157-158),

(iii) The angular diameters in the sky of the shadows on the primary (equations 155 and 164), and

(iv) The transverse distance of an observer who is able to see a double annular eclipse (equations 165-170).

ACKNOWLEDGEMENTS

I thank the referee for their careful reading of the manuscript and their thoughtful and astute comments, which have led to clear improvements. I gratefully acknowledge the support of the STFC via an Ernest Rutherford Fellowship (grant ST/P003850/1).

REFERENCES

Agol, E., Steffen, J., Sari, R., & Clarkson, W. 2005, MNRAS, 359, 567
Agol, E., & Deck, K. 2016, ApJ, 818, 177
Agol, E., & Fabrycky, D. C. 2017, Handbook of Exoplanets, Edited by Hans J. Deeg and Juan Antonio Belmonte. Springer Living Reference Work, ISBN: 978-3-319-30648-3, 2017, id.7
Berzosa Molina, J., Rossi, L., & Stam, D. M. 2018, In Press A&A, arXiv:1807.10266
Brakensiek, J., & Ragozzine, D. 2016, ApJ, 821, 47
Cabrera, J., & Schneider, J. 2007, A&A, 464, 1133
Cayley, A. 1870, MNRAS, 30, 166
Chambers, J. E. 1999, MNRAS, 304, 793
Colwell, J. E., Esposito, L. W., & Cooney, J. H. 2018, Icarus, 300, 150
Coolidge, J. L. 1968, A History of the Conic Sections and Quadric Surfaces, Dover Publications, Inc. New York.
Deck, K. M., & Agol, E. 2015, ApJ, 802, 116
Doolin, S., & Blundell, K. M. 2011, MNRAS, 418, 2656
Doyle, L. R., Carter, J. A., Fabrycky, D. C., et al. 2011, Science, 333, 1602
Farago, F., & Laskar, J. 2010, MNRAS, 401, 1189
Ford, E. B., Rowe, J. F., Fabrycky, D. C., et al. 2011, ApJS, 197, 2
Hadden, S., & Lithwick, Y. 2016, ApJ, 828, 44
Heller, R., & Pudritz, R. E. 2016, Astrobiology, 16, 259
Ismail, M. N., Bakry, A., Selim, H. H., Shehata, M. H. 2015, NRIAG Journal of Astronomy and Geophysics, 4, 117
Kawauchi, K., Narita, N., Sato, B., Hirano, T., Kawashima, Y., Nakamoto, T., Yamashita, T., Tamura, M. 2018, PASJ, 70, 84
Kipping, D. M. 2008, MNRAS, 389, 1383
Kipping, D. M. 2010, MNRAS, 407, 301
Kostov, V. B., McCullough, P. R., Carter, J. A., et al. 2014, ApJ, 784, 14
Lithwick, Y., Xie, J., & Wu, Y. 2012, ApJ, 761, 122
Luger, R., Lustig-Yaeger, J., & Agol, E. 2017, ApJ In Press, arXiv:1711.05739
Mardling, R. A. 2010, MNRAS, 407, 1048
Martin, D. V. 2017a, MNRAS, 465, 3235
Martin, D. V. 2017b, MNRAS, 467, 1694
Martin, D. V., & Triaud, A. H. M. J. 2015, MNRAS, 449, 781
McCrea, W. H. Analytical Geometry of Three Dimensions. Edinburgh: Oliver and Boyd
Mentel, R. T., Kenworthy, M. A., Cameron, D. A., et al. 2018, In Press A&A, arXiv:1810.05171
Morris, S. L. 1999, ApJ, 520, 797
Nesvorný, D., & Morbidelli, A. 2008, ApJ, 688, 636-646
Nesvorný, D. 2009, ApJ, 701, 1116
Ortiz, J. L., Santos-Sanz, P., Sicardy, B., et al. 2017, Nature, 550, 219
Read, M. J., Wyatt, M. C., & Triaud, A. H. M. J. 2017, MNRAS, 469, 171
Rigge, W. F. 1924, The graphic construction of eclipses and occultations. Chicago, Ill., Loyola University Press
Roy, A. E. 2005, Orbital motion / A. E. Roy. Bristol (UK): Institute of Physics Publishing, 4th edition.
Schneider, J., & Chevreton, M. 1990, A&A, 232, 251
Schneider, J. 1994, P&SS, 42, 539
Seager, S., & Mallén-Ornelas, G. 2003, ApJ, 585, 1038
Sigurdsson, S. 1993, ApJL, 415, L43
Sigurdsson, S., Richer, H. B., Hansen, B. M., Stairs, I. H., & Thorsett, S. E. 2003, Science, 301, 193
Smith, C. Solid Geometry. London: Macmillian and Co.
Stevens, D. J., & Gaudi, B. S. 2013, PASP, 125, 933
Teachey, A., & Kipping, D. M. 2018, arXiv:1810.02362
Thorsett, S. E., Arzoumanian, Z., & Taylor, J. H. 1993, ApJL, 412, L33
Tingley, B., & Sackett, P. D. 2005, ApJ, 627, 1011
The Astronomical Almanac. Published by Her Majesty's Nautical Almanac Office and United States Naval Observatory 2018.
Veras, D. 2014, Celestial Mechanics and Dynamical Astronomy, 118, 315

Veras, D., & Breedt, E. 2017, MNRAS, 468, 2672
Wells, R., Poppenhaeger, K., Watson, C. A., & Heller, R. 2018, MNRAS, 473, 345
Winn, J. N., arXiv:1001.2010
Zwillinger, D. 1996, CRC Standard Mathematical Tables and Formulae, 30th ed. Boca Raton, FL: CRC Press, pp. 316-319.

APPENDIX A: CARTESIAN ELEMENTS FOR TIME EVOLUTIONS

In this appendix I provide explicit expressions for Cartesian elements in terms of orbital elements and time for all of the architectures seen in Figs. 1 and 2. The goal in every case is to derive expressions in terms of $x_{12}, y_{12}, z_{12}, x_{13}, y_{13}$, and z_{13} in terms of the masses and radii of the three bodies, and the orbital parameters from Table 6. These computations are performed through equations (1-6). The following equations represent useful references to expedite determinations of transit characteristics.

A1 Arbitrarily eccentric, coplanar orbits

I can impose coplanarity by assuming $i = w = \Omega = 0$ for each orbit. If a user wishes the plane of motion to not coincide with the z plane, then they can impose the appropriate rotation on the below expressions.

A1.1 One star and two planets (1S2P)

$$x^{(e)}_{12,\ 1S2P} = \frac{a_{12}\left(1-e_{12}^2\right)}{1+e_{12}\cos\Pi_{12}(t)}\cos\left[\mathfrak{n}_{12}\left(t-\tau_{12}\right)\right], \tag{A1}$$

$$y^{(e)}_{12,\ 1S2P} = \frac{a_{12}\left(1-e_{12}^2\right)}{1+e_{12}\cos\Pi_{12}(t)}\sin\left[\mathfrak{n}_{12}\left(t-\tau_{12}\right)\right], \tag{A2}$$

$$z^{(e)}_{12,\ 1S2P} = 0, \tag{A3}$$

$$x^{(e)}_{13,\ 1S2P} = \frac{a_{13}\left(1-e_{13}^2\right)}{1+e_{13}\cos\Pi_{13}(t)}\cos\left[\mathfrak{n}_{13}\left(t-\tau_{13}\right)\right], \tag{A4}$$

$$y^{(e)}_{13,\ 1S2P} = \frac{a_{13}\left(1-e_{13}^2\right)}{1+e_{13}\cos\Pi_{13}(t)}\sin\left[\mathfrak{n}_{13}\left(t-\tau_{13}\right)\right], \tag{A5}$$

$$z^{(e)}_{13,\ 1S2P} = 0. \tag{A6}$$

A1.2 Two stars and one planet (2S1P)

$$x^{(e)}_{12,\ 2S1P} = x^{(e)}_{12,\ 1S2P}, \tag{A7}$$

$$y^{(e)}_{12,\ 2S1P} = y^{(e)}_{12,\ 1S2P}, \tag{A8}$$

$$z^{(e)}_{12,\ 2S1P} = 0, \tag{A9}$$

$$x^{(e)}_{13,\ 2S1P} = \frac{a_{123}\left(1-e_{123}^2\right)}{1+e_{123}\cos\Pi_{123}(t)}\cos\left[\mathfrak{n}_{123}\left(t-\tau_{123}\right)\right] + \left(\frac{M_1}{M_1+M_2}\right)x^{(e)}_{12,\ 1S2P}, \tag{A10}$$

$$y^{(e)}_{13,\ 2S1P} = \frac{a_{123}\left(1-e_{123}^2\right)}{1+e_{123}\cos\Pi_{123}(t)}\sin\left[\mathfrak{n}_{123}\left(t-\tau_{123}\right)\right] + \left(\frac{M_1}{M_1+M_2}\right)y^{(e)}_{12,\ 1S2P}, \tag{A11}$$

$$z^{(e)}_{13,\ 2S1P} = 0. \tag{A12}$$

A1.3 One moon, with moon occulter (1M–MO)

$$x^{(e)}_{12,\ 1M-MO} = x^{(e)}_{13,\ 1S2P} - \frac{a_{23}\left(1-e_{23}^2\right)}{1+e_{23}\cos\Pi_{23}(t)}\cos\left[\mathfrak{n}_{23}\left(t-\tau_{23}\right)\right], \tag{A13}$$

$$y^{(e)}_{12,\ 1M-MO} = y^{(e)}_{13,\ 1S2P} - \frac{a_{23}\left(1-e_{23}^2\right)}{1+e_{23}\cos\Pi_{23}(t)}\sin\left[\mathfrak{n}_{23}\left(t-\tau_{23}\right)\right], \tag{A14}$$

$$z^{(e)}_{12,\ 1M-MO} = 0, \tag{A15}$$

$$x^{(e)}_{13,\ 1M-MO} = x^{(e)}_{13,\ 1S2P}, \tag{A16}$$

$$y^{(e)}_{13,\ 1M-MO} = y^{(e)}_{13,\ 1S2P}, \tag{A17}$$

$$z^{(e)}_{13,\ 1M-MO} = 0. \tag{A18}$$

A1.4 One moon, with planet occulter (1M–PO)

$$x^{(e)}_{12,\ 1M-PO} = x^{(e)}_{12,\ 1S2P}, \tag{A19}$$

$$y^{(e)}_{12,\ 1M-PO} = y^{(e)}_{12,\ 1S2P}, \tag{A20}$$

$$z^{(e)}_{12,\ 1M-PO} = 0, \tag{A21}$$

$$x^{(e)}_{13,\ 1M-PO} = x^{(e)}_{12,\ 1S2P} + \frac{a_{23}\left(1-e_{23}^2\right)}{1+e_{23}\cos\Pi_{23}(t)}\cos\left[\mathfrak{n}_{23}\left(t-\tau_{23}\right)\right], \tag{A22}$$

$$y^{(e)}_{13,\ 1M-PO} = y^{(e)}_{12,\ 1S2P} + \frac{a_{23}\left(1-e_{23}^2\right)}{1+e_{23}\cos\Pi_{23}(t)}\sin\left[\mathfrak{n}_{23}\left(t-\tau_{23}\right)\right], \tag{A23}$$

$$z^{(e)}_{13,\ 1M-PO} = 0. \tag{A24}$$

A2 Circular, arbitrarily inclined orbits

Circular orbits imply $r(t) = a$, and hence eliminates a time dependence that is present with eccentric orbits. Instead the time dependence arises within the orbital angles as follows:

A2.1 One star and two planets (1S2P)

$$x^{(i)}_{12,\ 1S2P} = a_{12}\left[\mathcal{C}_{12}\cos\Omega_{12} - \mathcal{S}_{12}\cos i_{12}\sin\Omega_{12}\right], \tag{A25}$$

$$y^{(i)}_{12,\ 1S2P} = a_{12}\left[\mathcal{C}_{12}\sin\Omega_{12} + \mathcal{S}_{12}\cos i_{12}\cos\Omega_{12}\right], \tag{A26}$$

$$z^{(i)}_{12,\ 1S2P} = a_{12}\mathcal{S}_{12}\sin i_{12}, \tag{A27}$$

$$x^{(i)}_{13,\ 1S2P} = a_{13}\left[\mathcal{C}_{13}\cos\Omega_{13} - \mathcal{S}_{13}\cos i_{13}\sin\Omega_{13}\right], \tag{A28}$$

$$y^{(\mathrm{i})}_{13,\ 1\mathrm{S2P}} = a_{13}\left[\mathcal{C}_{13}\sin\Omega_{13} + \mathcal{S}_{13}\cos i_{13}\cos\Omega_{13}\right], \tag{A29}$$

$$z^{(\mathrm{i})}_{13,\ 1\mathrm{S2P}} = a_{13}\mathcal{S}_{13}\sin i_{13}. \tag{A30}$$

A2.2 Two stars and one planet (2S1P)

$$x^{(\mathrm{i})}_{12,\ 2\mathrm{S1P}} = x^{(\mathrm{i})}_{12,\ 1\mathrm{S2P}}, \tag{A31}$$

$$y^{(\mathrm{i})}_{12,\ 2\mathrm{S1P}} = y^{(\mathrm{i})}_{12,\ 1\mathrm{S2P}}, \tag{A32}$$

$$z^{(\mathrm{i})}_{12,\ 2\mathrm{S1P}} = z^{(\mathrm{i})}_{12,\ 1\mathrm{S2P}}, \tag{A33}$$

$$x^{(\mathrm{i})}_{13,\ 2\mathrm{S1P}} = a_{123}\left[\mathcal{C}_{123}\cos\Omega_{123} - \mathcal{S}_{123}\cos i_{123}\sin\Omega_{123}\right] + \left(\frac{M_1}{M_1+M_2}\right) x^{(\mathrm{i})}_{12,\ 1\mathrm{S2P}}, \tag{A34}$$

$$y^{(\mathrm{i})}_{13,\ 2\mathrm{S1P}} = a_{123}\left[\mathcal{C}_{123}\sin\Omega_{123} + \mathcal{S}_{123}\cos i_{123}\cos\Omega_{123}\right] + \left(\frac{M_1}{M_1+M_2}\right) y^{(\mathrm{i})}_{12,\ 1\mathrm{S2P}}, \tag{A35}$$

$$z^{(\mathrm{i})}_{13,\ 2\mathrm{S1P}} = a_{123}\mathcal{S}_{123}\sin i_{123} + \left(\frac{M_1}{M_1+M_2}\right) z^{(\mathrm{i})}_{12,\ 1\mathrm{S2P}}. \tag{A36}$$

A2.3 One moon, with moon occulter (1M–MO)

$$x^{(\mathrm{i})}_{12,\ 1\mathrm{M-MO}} = x^{(\mathrm{i})}_{13,\ 1\mathrm{S2P}} - a_{23}\left[\mathcal{C}_{23}\cos\Omega_{23} - \mathcal{S}_{23}\cos i_{23}\sin\Omega_{23}\right], \tag{A37}$$

$$y^{(\mathrm{i})}_{12,\ 1\mathrm{M-MO}} = y^{(\mathrm{i})}_{13,\ 1\mathrm{S2P}} - a_{23}\left[\mathcal{C}_{23}\sin\Omega_{23} + \mathcal{S}_{23}\cos i_{23}\cos\Omega_{23}\right], \tag{A38}$$

$$z^{(\mathrm{i})}_{12,\ 1\mathrm{M-MO}} = z^{(\mathrm{i})}_{13,\ 1\mathrm{S2P}} - a_{23}\mathcal{S}_{23}\sin i_{23}, \tag{A39}$$

$$x^{(\mathrm{i})}_{13,\ 1\mathrm{M-MO}} = x^{(\mathrm{i})}_{13,\ 1\mathrm{S2P}}, \tag{A40}$$

$$y^{(\mathrm{i})}_{13,\ 1\mathrm{M-MO}} = y^{(\mathrm{i})}_{13,\ 1\mathrm{S2P}}, \tag{A41}$$

$$z^{(\mathrm{i})}_{13,\ 1\mathrm{M-MO}} = z^{(\mathrm{i})}_{13,\ 1\mathrm{S2P}}. \tag{A42}$$

A2.4 One moon, with planet occulter (1M–PO)

$$x^{(\mathrm{i})}_{12,\ 1\mathrm{M-PO}} = x^{(\mathrm{i})}_{12,\ 1\mathrm{S2P}}, \tag{A43}$$

$$y^{(\mathrm{i})}_{12,\ 1\mathrm{M-PO}} = y^{(\mathrm{i})}_{12,\ 1\mathrm{S2P}}, \tag{A44}$$

$$z^{(\mathrm{i})}_{12,\ 1\mathrm{M-PO}} = z^{(\mathrm{i})}_{12,\ 1\mathrm{S2P}}, \tag{A45}$$

$$x^{(\mathrm{i})}_{13,\ 1\mathrm{M-PO}} = x^{(\mathrm{i})}_{12,\ 1\mathrm{S2P}} + a_{23}\left[\mathcal{C}_{23}\cos\Omega_{23} - \mathcal{S}_{23}\cos i_{23}\sin\Omega_{23}\right], \tag{A46}$$

$$y^{(\mathrm{i})}_{13,\ 1\mathrm{M-PO}} = y^{(\mathrm{i})}_{12,\ 1\mathrm{S2P}} + a_{23}\left[\mathcal{C}_{23}\sin\Omega_{23} + \mathcal{S}_{23}\cos i_{23}\cos\Omega_{23}\right], \tag{A47}$$

$$z^{(\mathrm{i})}_{13,\ 1\mathrm{M-PO}} = z^{(\mathrm{i})}_{12,\ 1\mathrm{S2P}} + a_{23}\mathcal{S}_{23}\sin i_{23}. \tag{A48}$$

A3 Circular, coplanar orbits

In the simplest case, the equations are the most compact of the three example geometries considered.

A3.1 One star and two planets (1S2P)

$$x^{(\mathrm{cc})}_{12,\ 1\mathrm{S2P}} = a_{12}\cos\left[\mathfrak{n}_{12}\left(t-\tau_{12}\right)\right], \tag{A49}$$

$$y^{(\mathrm{cc})}_{12,\ 1\mathrm{S2P}} = a_{12}\sin\left[\mathfrak{n}_{12}\left(t-\tau_{12}\right)\right], \tag{A50}$$

$$z^{(\mathrm{cc})}_{12,\ 1\mathrm{S2P}} = 0, \tag{A51}$$

$$x^{(\mathrm{cc})}_{13,\ 1\mathrm{S2P}} = a_{13}\cos\left[\mathfrak{n}_{13}\left(t-\tau_{13}\right)\right], \tag{A52}$$

$$y^{(\mathrm{cc})}_{13,\ 1\mathrm{S2P}} = a_{13}\sin\left[\mathfrak{n}_{13}\left(t-\tau_{13}\right)\right], \tag{A53}$$

$$z^{(\mathrm{cc})}_{13,\ 1\mathrm{S2P}} = 0. \tag{A54}$$

A3.2 Two stars and one planet (2S1P)

$$x^{(\mathrm{cc})}_{12,\ 2\mathrm{S1P}} = x^{(\mathrm{cc})}_{12,\ 1\mathrm{S2P}}, \tag{A55}$$

$$y^{(\mathrm{cc})}_{12,\ 2\mathrm{S1P}} = y^{(\mathrm{cc})}_{12,\ 1\mathrm{S2P}}, \tag{A56}$$

$$z^{(\mathrm{cc})}_{12,\ 2\mathrm{S1P}} = 0, \tag{A57}$$

$$x^{(\mathrm{cc})}_{13,\ 2\mathrm{S1P}} = a_{123}\cos\left[\mathfrak{n}_{123}\left(t-\tau_{123}\right)\right] + \left(\frac{M_1}{M_1+M_2}\right) x^{(\mathrm{cc})}_{12,\ 1\mathrm{S2P}}, \tag{A58}$$

$$y^{(\mathrm{cc})}_{13,\ 2\mathrm{S1P}} = a_{123}\sin\left[\mathfrak{n}_{123}\left(t-\tau_{123}\right)\right] + \left(\frac{M_1}{M_1+M_2}\right) y^{(\mathrm{cc})}_{12,\ 1\mathrm{S2P}}, \tag{A59}$$

$$z^{(\mathrm{cc})}_{13,\ 2\mathrm{S1P}} = 0. \tag{A60}$$

A3.3 One moon, with moon occulter (1M–MO)

$$x^{(\mathrm{cc})}_{12,\ 1\mathrm{M-MO}} = x^{(\mathrm{cc})}_{13,\ 1\mathrm{S2P}} - a_{23}\cos\left[\mathfrak{n}_{23}\left(t-\tau_{23}\right)\right], \tag{A61}$$

$$y^{(\mathrm{cc})}_{12,\ 1\mathrm{M-MO}} = y^{(\mathrm{cc})}_{13,\ 1\mathrm{S2P}} - a_{23}\sin\left[\mathfrak{n}_{23}\left(t-\tau_{23}\right)\right], \tag{A62}$$

$$z^{(\mathrm{cc})}_{12,\ 1\mathrm{M-MO}} = 0, \tag{A63}$$

$$x^{(\mathrm{cc})}_{13,\ 1\mathrm{M-MO}} = x^{(\mathrm{cc})}_{13,\ 1\mathrm{S2P}}, \tag{A64}$$

$$y^{(\mathrm{cc})}_{13,\ 1\mathrm{M-MO}} = y^{(\mathrm{cc})}_{13,\ 1\mathrm{S2P}}, \tag{A65}$$

$$z^{(\mathrm{cc})}_{13,\ 1\mathrm{M-MO}} = 0. \tag{A66}$$

A3.4 One moon, with planet occulter (1M–PO)

$$x^{(\mathrm{cc})}_{12,\ 1\mathrm{M-PO}} = x^{(\mathrm{cc})}_{12,\ 1\mathrm{S2P}}, \tag{A67}$$

$$y^{(\mathrm{cc})}_{12,\ 1\mathrm{M-PO}} = y^{(\mathrm{cc})}_{12,\ 1\mathrm{S2P}}, \tag{A68}$$

$$z^{(\mathrm{cc})}_{12,\ 1\mathrm{M-PO}} = 0, \tag{A69}$$

$$x^{(\mathrm{cc})}_{13,\ 1\mathrm{M-PO}} = x^{(\mathrm{cc})}_{12,\ 1\mathrm{S2P}} + a_{23}\cos\left[\mathfrak{n}_{23}\left(t-\tau_{23}\right)\right], \tag{A70}$$

$$y^{(cc)}_{13,\ 1M-PO} = y^{(cc)}_{12,\ 1S2P} + a_{23}\sin\left[\mathfrak{n}_{23}\,(t-\tau_{23})\right], \quad \text{(A71)}$$

$$z^{(cc)}_{13,\ 1M-PO} = 0. \quad \text{(A72)}$$

APPENDIX B: GOODNESS OF STATIC ORBIT APPROXIMATION

When deriving relations for orbital motion in Section 8, I assumed that the bodies move along static orbits. In reality, mutual three-body gravitational effects perturb these orbits, as well as altering the speed of the bodies which traverse these orbits. Hence, the applicability of my relations for motion depend on (i) the architecture considered, (ii) the accuracy sought, and (iii) the timescale over which the results are to be generated.

In this appendix, I provide some quantitative context for this applicability. I compute the extent of the departure between the static and perturbed cases for just a few representative architectures. I do so by performing multi-body numerical simulations with point-mass bodies. Their outcomes generate (x, y, z) locations of an object at a series of times, and I calculate the distance from these locations to the locations analytically obtained from the formulae in Section 8 and Appendix A at those same times. This time-dependent distance is henceforth denoted as *deviation*. The maximum deviation would then represent approximately the longest axis of the initial orbit.

For my numerical simulations, I used the Bulirsch-Stoer integrator from the *Mercury* integration package (Chambers 1999) with an accuracy tolerance of 10^{-12}. This integrator utilises a variable timestep and so is adaptable to all of the architectures considered here, but does suffer from floating point round-off error. Throughout I adopted $1M_{\odot}$ stars and set the output time interval to be at most a few per cent of the orbital period of the smallest orbit, but not small enough to resolve variations during an individual transit. I ran the simulations for no longer than a few human lifetimes, but sufficiently long enough to sample tens, hundreds or thousands of transits depending on architecture. I started with the orbital elements in Table 6 and subsequently converted them into Cartesian elements for input into the code.

For consistency, the numerical constants which I inserted into the analytics needed to be equivalent to those in the code. Hence, I adopted *Mercury's* now slightly-outdated value for the astronomical unit (149597870000 m), its value for Solar mass (1.9891×10^{30} kg), its definition of year (365.25 days) and its value for $\mathfrak{G}$ – obtained through the code representation of `K2` – of $6.67198422296 \times 10^{-11}$ N·kg^{-2}·m^2.

B1 The 1S2P case

Two planets orbiting one star may be subject to a variety of secular and mean motion resonances. These resonances are encountered at particular planet separations and orbital angles. Generally, however, the larger the initial separation, the smaller the magnitude of the perturbation, particularly on timescales of tens or hundreds of orbits.

I present deviations for a variety of two-planet, one-star, circular, coplanar (cc) case instances in Fig. B1. The curves in the figure are not solid lines, but rather contain oscillations at different scales and so appear fuzzy.

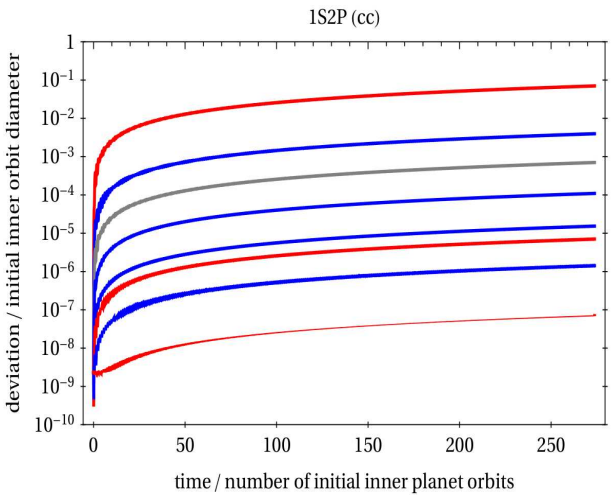

Figure B1. For the 1S2P circular, coplanar (cc) case, shown is the separation between the location of an inner planet within a gravitational three-body simulation and the location of an inner planet whose time evolution is dictated by the analytical formulae from Section 8 and Appendix A. Here, $M_1 = M_{\odot}$ and $a_{12} = 1$ au. The blue and gray curves all share $M_2 = M_3 = 10^{-6}M_1$, with, from top to bottom, initial $a_{13}/a_{12} = 1.5, 2.0, 3.0, 5.0$ and 10.0. The red and gray curves all share $a_{13}/a_{12} = 2.0$, with, from top to bottom, $M_2/M_1 = M_3/M_1 = 10^{-4}, 10^{-6}, 10^{-8}$ and 10^{-10}.

In all instances, the inner planet was initially located at 1 au and the two planets were of equal mass. The gray curve (third from top) represents a type of fiducial case for close orbits, with $M_2 = M_3 = 10^{-6}M_1$ and $a_{13}/a_{12} = 2$ (initially). The red curves then keep this same initial semimajor axis ratio but sample different masses: $M_2 = M_3 = 10^{-4}M_1$ (top curve), $M_2 = M_3 = 10^{-8}M_1$ (third from bottom curve), and $M_2 = M_3 = 10^{-10}M_1$ (bottom curve). The blue curves keep $M_2 = M_3 = 10^{-6}M_1$ but vary the initial mutual separations as $a_{13}/a_{12} = 1.5$ (second from top curve), 3 (fourth from top curve), 5 (fourth from bottom curve) and 10 (second from bottom curve).

These curves do not sample the entire range of known separations. For example, the semimajor axis ratio of Neptune and Mercury is about 78. On the lower end, semimajor axis ratios much smaller than 1.5 are subject to dynamical instabilities depending on the planet masses and other orbital parameters.

B2 The 2S1P case

2S1P architectures are more prone to the effects of precession than in the 1S2P case. For eccentric and/or inclined orbits, both stars can quickly precess the outer orbit's argument of pericentre and quickly regress the outer orbit's longitude of ascending node. Even in the circular, coplanar case, there will be short-term variations of the osculating elements, and in a more pronounced way than in the 1S2P circular coplanar case. Quick orbital changes explain why circumbinary exoplanets like Kepler-413 ABb disappeared and re-appeared during the original *Kepler* mission (Kostov et al. 2014).

Fig. B2 presents five curves of deviations, all of which feature a planet mass of $M_3 = 10^{-6}M_2 = 10^{-6}M_1$ and an

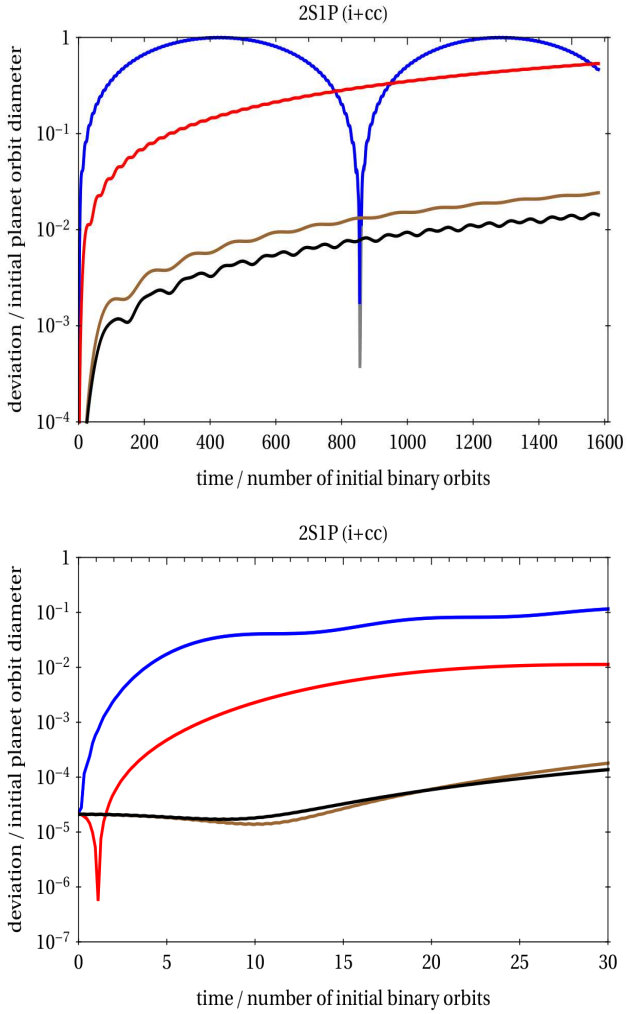

Figure B2. Deviations like those in Fig. B1, except for the 2S1P case. The circular, coplanar case is given by the gray curves (which are mostly under the blue curves), and the circular, inclined case is given by the other curves. The bottom plot is a zoom-in of the top plot for the first 30 binary orbits. Here, $M_1 = M_2 = M_\odot$, $M_3 = 10^{-6} M_1$, and $a_{12} = 0.2$ au, $i_{12} = 0°$. The five curves from top to bottom correspond to ($a_{123} = 1$ au, $i_{123} = 0°$; gray), ($a_{123} = 1$ au, $i_{123} = 1°$; blue), ($a_{123} = 2$ au, $i_{123} = 1°$; red), ($a_{123} = 5$ au, $i_{123} = 1°$; brown), and ($a_{123} = 5$ au, $i_{123} = 50°$; black).

initial inner binary semimajor axis of $a_{12} = 0.2$ au. Both orbits were initially circular, and in all cases $i_{12} = 0°$, $\Omega_{12} = \Omega_{123} = 0°$. The outer orbit initial semimajor axis and inclination for the curves, from top to bottom, were respectively, ($a_{123} = 1$ au, $i_{123} = 0°$ for gray), ($a_{123} = 1$ au, $i_{123} = 1°$ for blue), ($a_{123} = 2$ au, $i_{123} = 1°$ for red), ($a_{123} = 5$ au, $i_{123} = 1°$ for brown), and ($a_{123} = 5$ au, $i_{123} = 50°$ for black). The bottom plot is a zoom-in of the top plot for the first 30 binary eclipses. The blue and gray curves are nearly coincident, except for the trough or kink in the top plot.

The initially 1 au planet achieved a maximum deviation after about 400 initial binary orbits, and then repeated this behaviour in a cyclical pattern. Alternatively, the initially 2 au planet did not reach maximum deviation until after 1600 initial binary orbits, demonstrating a strong dependence of deviation on a_{123}. In contrast, the dependence on inclination is relatively weak, as shown by the blue, brown, gray and black curves. The differences in deviation are easily discernable between the $i_{123} = 1°$ and $i_{123} = 50°$ cases, at least after several tens of binary orbits. The difference in deviation between the $i_{123} = 0°$ and $i_{123} = 1°$ cases, however, is discernable only at the kink. This kink represents the location where the orbit has precessed through a complete revolution, such that the deviation returns close to zero for a relatively short time. The deviation stretches closer to zero in the coplanar case (gray curve) than in the inclined case (blue curve). The inclination differences ultimately indicate that the orbital changes cannot be dominated by nodal precession.

These dependencies have been well-studied analytically in the limiting cases of $M_3 = 0$ and for averaged, or secular, orbits. In these limits, perturbation theory can be used to approximate the time evolution of Ω_{123} as a series (see Eq. 208 of Veras 2014), the leading term of which is similar to leading term of the time evolution of w_{123} (see Eq. 212 of Veras 2014). An alternate expression for this leading term, expressed as a precession timescale, can be found in Eq. 15 of Martin (2017a), having originated from the studies of Schneider (1994), Farago & Laskar (2010) and Doolin & Blundell (2011).

The availability of analytic approximations for secular precession timescales, combined with the periodic behaviour of the curves in Fig. B2 (apparent in the top two curves of the top plot only), potentially allows one to provide a correction term to the analytical treatment in this paper. Doing so may reduce deviations, particularly for the planets with the smallest orbits.

B3 The 1M-MO case

A moon with a planet host which is close to its parent star might be subject to similarly fast orbit precession (see Eq. 3 of Martin 2017b, and Mardling 2010), leading to large deviations on short timescales. In order to explore this possibility within the context of my 1M-MO case, I considered a (giant) planet with mass $M_3 = 10^{-3} M_\odot$ which hosts a moon of mass $M_2 = 10^{-8} M_\odot$ on an inclined circular orbit with respect to $i_{23} = 0°$. I chose a large initial satellite distance of $a_{23} = 10^6$ km in order to test an extreme-case scenario of least accuracy. This distance still however lies within the Hill sphere of all sampled semimajor axes (described below), meaning that the moon orbits the planet and not the star. On the other extreme, a moon like Phobos resides just 6000 km from Mars, with resulting deviations which may be significantly lower (see Eq. 3 of Martin 2017b).

Figure B3 illustrates the results with three pairs of curves. The three pairs from top to bottom correspond to initial values of $a_{13} = 0.5, 1.0$ and 5.0 au. The blue curves illustrate the case of an initial value of $i_{13} = 1°$ whereas the red curves showcase an initial value of $i_{13} = 50°$. The deviations again illustrate a weak dependence on inclination and a stronger dependence on a_{13}.

B4 Regions of validity

The plots in this Appendix suggest that the static orbit approximation cannot be used on timescales at or beyond

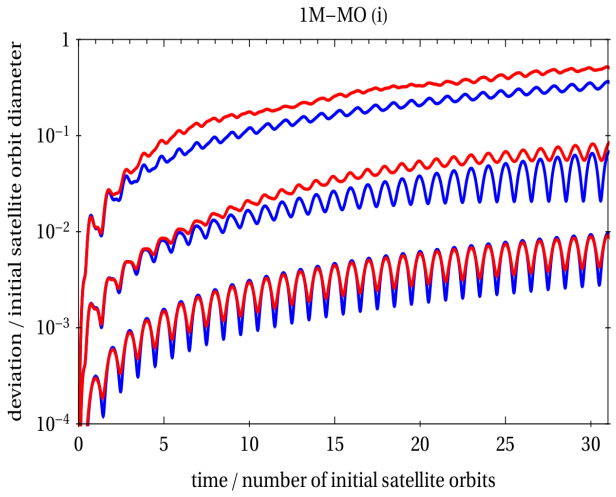

Figure B3. Deviations like those in Figs. B1 and B2, except for the 1M-MO inclined (i) case. Here, $M_1 = M_\odot, M_2 = 10^{-8} M_\odot$, $M_3 = 10^{-3} M_\odot$, and $a_{23} = 10^6$ km, $i_{23} = 0°$. The top, middle and bottom pairs of curves correspond to $a_{13} = 0.5, 1.0$ and 5.0 au. The blue and red curves respectively correspond to initial values of $i_{13} = 1°$ and $50°$.

which a curve reaches unity, unless correction terms are applied. Consider the top (blue) curve in Fig. B2, which reaches unity after about 400 binary orbits. Although this case is representative of most currently known circumbinary exoplanets, as more distant exoplanets are discovered orbiting two stars, the fixed-orbit approximation will become more useful.

Up until what time is the static orbit approximation then applicable? The answer depends on the user's motivation, the accuracy they seek, the deviation of the other bodies in the system, and how all deviations are broken down into (x, y, z) components. For example, for those wishing to compute a single transit duration – which is a small fraction of one orbit– the resulting accuracy can vary by at least eight orders of magnitude depending on which of the small sample of architectures considered here is chosen.

In general, however, some trends have emerged. The static orbit approximation is better suited to the 1S2P case than the 2S1P and 1M-MO cases. Also, distant transits tend to reduce deviations. More precisely, large mutual separations of three bodies will improve the static orbit approximation. Overall, the static orbit approximation is better used to approximate transit durations and frequencies rather than predict actual instances of eclipses for sufficiently massive objects residing within about 10 au of their parent star or stars.